COSMOLOGICAL CONSTRAINTS FROM GALAXY CLUSTERS IN THE 2500 SQUARE-DEGREE SPT-SZ SURVEY

The Astrophysical Journal, 832:95 (17pp), 2016 November 20 doi:10.3847/0004-637X/832/1/95

COSMOLOGICAL CONSTRAINTS FROM GALAXY CLUSTERS IN THE 2500 SQUARE-DEGREE SPT-SZ SURVEY

T. de Haan[1,2], B. A. Benson[3,4,5], L. E. Bleem[4,6,7], S. W. Allen[8,9,10], D. E. Applegate[11], M. L. N. Ashby[12], M. Bautz[13], M. Bayliss[12,14], S. Bocquet[4,7,15,16], M. Brodwin[17], J. E. Carlstrom[3,4,6,7,18], C. L. Chang[3,4,7], I. Chiu[15,16], H-M. Cho[19], A. Clocchiatti[20], T. M. Crawford[3,4], A. T. Crites[3,4,21], S. Desai[15,16], J. P. Dietrich[15,16], M. A. Dobbs[2,22], A. N. Doucouliagos[23], R. J. Foley[24,25], W. R. Forman[12], G. P. Garmire[26], E. M. George[1,27], M. D. Gladders[3,4], A. H. Gonzalez[28], N. Gupta[15,16], N. W. Halverson[29], J. Hlavacek-Larrondo[9,30,31], H. Hoekstra[32], G. P. Holder[2], W. L. Holzapfel[1], Z. Hou[4,6], J. D. Hrubes[33], N. Huang[1], C. Jones[12], R. Keisler[4,6,8,9], L. Knox[34], A. T. Lee[1,35], E. M. Leitch[3,4], A. von der Linden[8,9,36,37], D. Luong-Van[33], A. Mantz[4,8,9], D. P. Marrone[38], M. McDonald[13], J. J. McMahon[39], S. S. Meyer[3,4,6,18], L. M. Mocanu[3,4], J. J. Mohr[15,16,27], S. S. Murray[12], S. Padin[3,4,21], C. Pryke[40], D. Rapetti[15,16], C. L. Reichardt[23], A. Rest[41], J. Ruel[14], J. E. Ruhl[42], B. R. Saliwanchik[42], A. Saro[15,16], J. T. Sayre[29], K. K. Schaffer[4,18,43], T. Schrabback[11], E. Shirokoff[3,4], J. Song[39,44], H. G. Spieler[35], B. Stalder[12], S. A. Stanford[34,45], Z. Staniszewski[42], A. A. Stark[12], K. T. Story[8,9], C. W. Stubbs[12,14], K. Vanderlinde[46,47], J. D. Vieira[24,25], A. Vikhlinin[12], R. Williamson[3,4,21], and A. Zenteno[48]

[1] Department of Physics, University of California, Berkeley, CA 94720, USA
[2] Department of Physics,McGill University, Montreal, Quebec H3A 2T8, Canada
[3] Department of Astronomy and Astrophysics, University of Chicago, Chicago, IL 60637, USA
[4] Kavli Institute for Cosmological Physics, University of Chicago, Chicago, IL 60637, USA
[5] Fermi National Accelerator Laboratory, Batavia, IL 60510-0500, USA
[6] Department of Physics, University of Chicago, Chicago, IL 60637, USA
[7] Argonne National Laboratory, Argonne, IL 60439, USA
[8] Kavli Institute for Particle Astrophysics and Cosmology, Stanford University, 452 Lomita Mall, Stanford, CA 94305, USA
[9] Department of Physics, Stanford University, 382 Via Pueblo Mall, Stanford, CA 94305, USA
[10] SLAC National Accelerator Laboratory, 2575 Sand Hill Road, Menlo Park, CA 94025, USA
[11] Argelander-Institut für Astronomie, Auf dem Hügel 71, D-53121 Bonn, Germany
[12] Harvard-Smithsonian Center for Astrophysics, Cambridge, MA 02138, USA
[13] Kavli Institute for Astrophysics and Space Research, Massachusetts Institute of Technology, 77 Massachusetts Avenue, Cambridge, MA 02139, USA
[14] Department of Physics, Harvard University, 17 Oxford Street, Cambridge, MA 02138, USA
[15] Faculty of Physics, Ludwig-Maximilians-Universität, Scheinerstr. 1, D-81679 Munich, Germany
[16] Excellence Cluster universe, Boltzmannstr. 2, D-85748 Garching, Germany
[17] Department of Physics and Astronomy, University of Missouri, 5110 Rockhill Road, Kansas City, MO 64110, USA
[18] Enrico Fermi Institute, University of Chicago, Chicago, IL 60637, USA
[19] NIST Quantum Devices Group, Boulder, CO 80305, USA
[20] Departamento de Astronomia y Astrosifica, Pontificia Universidad Catolica, Chile
[21] California Institute of Technology, Pasadena, CA 91125, USA
[22] Canadian Institute for Advanced Research, CIFAR Program in Cosmology and Gravity, Toronto, ON, M5G 1Z8, Canada
[23] School of Physics, University of Melbourne, Parkville, VIC 3010, Australia
[24] Astronomy Department, University of Illinois at Urbana-Champaign, 1002 W. Green Street, Urbana, IL 61801, USA
[25] Department of Physics, University of Illinois Urbana-Champaign, 1110 W. Green Street, Urbana, IL 61801, USA
[26] Huntingdon Institute for X-ray Astronomy, LLC, Huntingdon, PA 16652, USA
[27] Max Planck Institute for Extraterrestrial Physics, Giessenbachstr. 1, D-85748 Garching, Germany
[28] Department of Astronomy, University of Florida, Gainesville, FL 32611, USA
[29] Department of Astrophysical and Planetary Sciences and Department of Physics, University of Colorado, Boulder, CO 80309, USA
[30] Department of Physics, Université de Montréal, Montrea, Quebec H3T 1J4, Canada
[31] Kavli Institute for Particle Astrophysics and Cosmology, Stanford University, 452 Lomita Mall, Stanford, CA 94305-4085, USA
[32] Leiden Observatory, Leiden University, Niels Bohrweg 2, 2333 CA, Leiden, The Netherlands
[33] University of Chicago, Chicago, IL 60637, USA
[34] Department of Physics, University of California, Davis, CA 95616, USA
[35] Physics Division, Lawrence Berkeley National Laboratory, Berkeley, CA 94720, USA
[36] Department of Physics and Astronomy, Stony Brook University, Stony Brook, NY 11794, USA
[37] Dark Cosmology Centre, Niels Bohr Institute, University of Copenhagen Juliane Maries Vej 30, DK-2100 Copenhagen, Denmark
[38] Steward Observatory, University of Arizona, 933 North Cherry Avenue, Tucson, AZ 85721, USA
[39] Department of Physics, University of Michigan, Ann Arbor, MI 48109, USA
[40] Department of Physics, University of Minnesota, Minneapolis, MN 55455, USA
[41] Space Telescope Science Institute, 3700 San Martin Dr., Baltimore, MD 21218, USA
[42] Physics Department, Center for Education and Research in Cosmology and Astrophysics, Case Western Reserve University, Cleveland, OH 44106, USA
[43] Liberal Arts Department, School of the Art Institute of Chicago, Chicago, IL 60603, USA
[44] Korea Astronomy and Space Science Institute, Daejeon 305-348, Korea
[45] Institute of Geophysics and Planetary Physics, Lawrence Livermore National Laboratory, Livermore, CA 94551, USA
[46] Dunlap Institute for Astronomy & Astrophysics, University of Toronto, 50 St George St, Toronto, ON, M5S 3H4, Canada
[47] Department of Astronomy & Astrophysics, University of Toronto, 50 St George St, Toronto, ON, M5S 3H4, Canada
[48] Cerro Tololo Inter-American Observatory, Casilla 603, La Serena, Chile

Received 2016 March 21; revised 2016 August 15; accepted 2016 September 7; published 2016 November 18

ABSTRACT

We present cosmological parameter constraints obtained from galaxy clusters identified by their Sunyaev–Zel'dovich effect signature in the 2500 square-degree South Pole Telescope Sunyaev Zel'dovich (SPT-SZ) survey.

We consider the 377 cluster candidates identified at $z > 0.25$ with a detection significance greater than five, corresponding to the 95% purity threshold for the survey. We compute constraints on cosmological models using the measured cluster abundance as a function of mass and redshift. We include additional constraints from multi-wavelength observations, including *Chandra* X-ray data for 82 clusters and a weak lensing-based prior on the normalization of the mass-observable scaling relations. Assuming a spatially flat ΛCDM cosmology, we combine the cluster data with a prior on H_0 and find $\sigma_8 = 0.784 \pm 0.039$ and $\Omega_m = 0.289 \pm 0.042$, with the parameter combination $\sigma_8 (\Omega_m/0.27)^{0.3} = 0.797 \pm 0.031$. These results are in good agreement with constraints from the cosmic microwave background (CMB) from SPT, *WMAP*, and *Planck*, as well as with constraints from other cluster data sets. We also consider several extensions to ΛCDM, including models in which the equation of state of dark energy w, the species-summed neutrino mass, and/or the effective number of relativistic species ($N_{\rm eff}$) are free parameters. When combined with constraints from the *Planck* CMB, H_0, baryon acoustic oscillation, and SNe, adding the SPT cluster data improves the w constraint by 14%, to $w = -1.023 \pm 0.042$.

Key words: cosmology: observations – galaxies: clusters: general

1. INTRODUCTION

Galaxy clusters trace extreme peaks in the matter density field on megaparsec scales. The abundance of these peaks as a function of mass and redshift is highly sensitive to the matter density and the growth of structure (e.g., Allen et al. 2011). As this abundance can be predicted with sufficient accuracy for a given cosmology (Holder & Carlstrom 2001; Tinker et al. 2008; Bhattacharya et al. 2011), even modest measurements of cluster abundance can yield powerful cosmological constraints. These constraints are particularly powerful when combined with or compared to independent constraints from probes such as the power spectrum of the cosmic microwave background (CMB) and baryon acoustic oscillations (BAOs). Taken together, growth-based and geometrical probes can place significantly tighter constraints on parameters such as the equation of state of dark energy than either one independently, because of nearly orthogonal parameter degeneracies. Considered independently, these constraints provide a consistency test of the dark energy paradigm and the validity of general relativity (Ishak et al. 2006; Mortonson et al. 2009, 2010; Rapetti et al. 2009, 2010; Zhan et al. 2009; Acquaviva & Gawiser 2010; Vanderveld et al. 2012).

In recent years, constraints on cosmological parameters from cluster abundance measurements have advanced significantly using cluster samples selected at X-ray (e.g., Vikhlinin et al. 2009b; Mantz et al. 2010, 2015), optical (e.g., Rozo et al. 2010), and millimeter (e.g., Hasselfield et al. 2013; Reichardt et al. 2013; Planck Collaboration et al. 2014b; Bocquet et al. 2015; Planck Collaboration et al. 2015) wavelengths. The predominant millimeter-wave (mm-wave) signal from clusters arises from the thermal Sunyaev–Zel'dovich (tSZ) effect (Sunyaev & Zel'dovich 1972), i.e., the scattering of CMB photons by hot electrons in the intracluster medium (ICM). The surface brightness of the tSZ effect is redshift-independent, allowing high-resolution mm-wave surveys to obtain nearly mass-limited samples of clusters to arbitrarily high redshift. The ability to cleanly select clusters out to the redshift at which dark energy begins to contribute significantly to the energy budget of the universe ($z \sim 1$) is particularly important for constraints on the dark energy equation of state and tests of the dark energy paradigm. Cluster surveys using high-resolution tSZ data are uniquely positioned to deliver such constraints (Carlstrom et al. 2002).

The primary limitation to cosmological constraints from current cluster surveys at all wavelengths is an imperfect understanding of the relationship between the quantity that can be predicted from theory or simulations (the cluster mass or the height of the associated density peak) and the observable property of the cluster that is used as a proxy for this quantity. The mass proxy can be the observable quantity used to construct the sample; it can also include observables from follow-up observations, often at different wavelengths than the cluster selection observable. Since the cluster abundance is an extremely steep function of mass, misestimation of the relation between the mass proxy and the true cluster mass can lead to significant biases on the resulting cosmological parameter constraints.

Different cluster mass proxies have distinct advantages and disadvantages related to the accuracy and precision with which they trace the true cluster mass and the expense of obtaining the data required to construct them. In terms of ultimate accuracy, or absence of bias, the current gold standard mass proxy is derived from measurements of weak gravitational lensing of background galaxies by clusters (see von der Linden et al. 2014b for a discussion). Optical mass measurements from weak gravitational lensing are observationally expensive to obtain at high redshift, and the scatter on individual cluster mass estimates is large. Gravitational lensing of the CMB by clusters is a promising future avenue for mass estimation (e.g., Baxter et al. 2015; Madhavacheril et al. 2015; Planck Collaboration et al. 2015). Cluster velocity dispersions, generally obtained through spectroscopic observations of tens of cluster member galaxies, are also mostly unaffected by complex ICM physics but are expensive observationally and have large scatter (e.g., Evrard et al. 2008; Saro et al. 2013; Sifón et al. 2013; Ruel et al. 2014), as well as uncertain velocity bias (e.g., Munari et al. 2013). Where weak lensing (WL) measurements provide high accuracy, measurements of the gas mass $M_{\rm gas}$, and/or of the integrated cluster pressure Y provide high precision. Estimated from tSZ or X-ray data, integrated cluster pressure is predicted and measured to track cluster mass with low scatter (e.g., Motl et al. 2005; Kravtsov et al. 2006; Nagai et al. 2007; Stanek et al. 2010), but its relation to true cluster mass can be complicated by non-thermal pressure support in clusters (e.g., Evrard et al. 1996; Nagai et al. 2007; Yu et al. 2015). Furthermore, robust Y estimates require either relatively high-quality X-ray data (to provide deprojected temperature and density profiles), or tSZ measurements with accurate information on all cluster scales (sub-arcminute scales to the virial radius). Mass proxies built from the same data used to select clusters, such as optical richness, X-ray luminosity, and tSZ detection significance, come at no extra cost but can demonstrate high scatter and require external calibration data to tie them robustly to the true cluster mass.

In this work, we use a sample of clusters derived from the SPT-SZ survey, a three-band mm-wave survey of 2500 deg^2 of the southern sky conducted with the South Pole Telescope (SPT, Carlstrom et al. 2011). The cluster selection method, redshift determination, and sample characteristics are described in detail in Bleem et al. (2015, hereafter B15). We use the mm-wave and redshift information from B15 in conjunction with targeted X-ray follow-up observations from *Chandra* to obtain cosmological constraints. The mass proxy we use is the tSZ detection significance ξ, calibrated using X-ray integrated pressure Y_X, which is in turn tied to true cluster mass using optical WL measurements.

The paper is organized as follows. In Section 2, we briefly describe the cluster sample, including the mm-wave data and analysis methods that went into producing the sample. We summarize the optical/infrared data and redshift estimation in Section 3, and the X-ray data and analysis methods in Section 4. The cosmological analysis methods are described in Section 5, and we present the cosmological parameter constraints in Section 6. We compare the cosmological constraints from this work to those from other cluster surveys in Section 7, and we conclude in Section 8.

When parameter constraints are reported, the best-fit value and uncertainties correspond to the mean and standard deviation of the posterior distribution. Cluster masses, denoted with M_Δ, refer to spherical overdensities for which the enclosed density is equal to Δ times the critical density, ρ_c. Similarly, r_Δ refers to the associated radius such that $M_\Delta = \frac{4}{3}\pi r_\Delta^3 \Delta \rho_c(z)$.

2. SZ DATA AND METHODS

The cluster sample used in this work is a subset of that previously presented in B15. We choose clusters with redshift $z > 0.25$ and detection significance $\xi > 5$. The significance cut was chosen such that the resulting catalog has high ($\sim$95%) purity, and the redshift cut allows for a nearly redshift-independent selection function (Vanderlinde et al. 2010, hereafter V10). Our strategy for tying the cluster abundance measurement to the cosmologically predicted halo mass function is to calibrate the SZ–mass scaling relation using *Chandra* X-ray measurements. The X-ray scaling relation is taken from Vikhlinin et al. (2009a, 2009b, hereafter V09), though we modify the overall normalization of this relation in Section 4.2 to be consistent with more recent WL measurements from Hoekstra et al. (2015, hereafter H15) and the Weighing the Giants (WtG) project (Applegate et al. 2014; von der Linden et al. 2014a; Mantz et al. 2015).

2.1. Sample of SZ Cluster Candidates

The SPT is a 10 m telescope located at the geographic South Pole. With a 1 degree field of view and $\sim$1 arcmin resolution, it was designed to rapidly map large areas of sky while being well matched to the angular size of high-redshift clusters. The SPT-SZ camera operated from 2007 through 2011 and consisted of a 960-element, photon-noise-limited bolometer array observing in three frequency bands centered at 95, 150, and 220 GHz, though this work uses only the first two bands. The observation strategy and analysis for the 2500 square-degree SPT-SZ survey are described in many previous SPT papers (e.g., Schaffer et al. 2011), and the analysis specific to obtaining the cluster sample is described in B15. Briefly, the majority of the 2500 square-degree survey was performed using the following scan strategy. The telescope is moved using a right-going scan in azimuth, followed by a left-going scan, followed by a step in elevation. This pattern is repeated until a $\gtrsim$100 square degree patch of sky is observed. One such iteration is termed an *observation*, whereas the patch of sky is termed a *field*. In the only exception to this observing strategy, for two thirds of the data taken on one field (ra21hdec-50), the scan pattern instead consisted of scans in elevation at a series of fixed azimuth positions. Each field was observed until a depth of $\lesssim$18 μK-arcmin at 150 GHz was reached. Table 1 lists the 19 fields that comprise the full survey. For more information on the properties of the fields, see Table 1 of B15.

Table 1
The 19 SPT-SZ Fields with the Simulation-derived Inputs to the Cosmological Analysis of the 2500 Square-degree Survey

Name	$\alpha_{\rm field}$	$\beta_{\rm field}$	$\gamma_{\rm field}$
RA5H30DEC-55	16.79	4.60	1.33
RA23H30DEC-55	17.58	4.03	1.39
RA21HDEC-60	25.64	4.07	1.29
RA3H30DEC-60	20.53	4.70	1.25
RA21HDEC-50	25.28	4.14	1.11
RA4H10DEC-50	16.75	5.48	1.27
RA0H50DEC-50	20.76	5.11	1.14
RA2H30DEC-50	14.98	4.78	1.19
RA1HDEC-60	17.25	5.38	1.18
RA5H30DEC-45	15.91	4.81	1.08
RA6H30DEC-55	17.77	4.58	1.16
RA3H30DEC-42.5	16.85	4.31	1.20
RA23HDEC-62.5	14.90	4.92	1.18
RA21HDEC-42.5	17.11	4.49	1.15
RA1HDEC-42.5	18.41	5.55	1.19
RA22H30DEC-55	16.45	5.23	1.13
RA23HDEC-45	17.00	5.20	1.19
RA6H30DEC-45	14.78	4.23	1.16
RA6HDEC-62.5	16.53	4.70	1.18

Note. The parameter $\alpha_{\rm field}$ describes the number of false detections expected above $\xi = 5$ scaled to 2500 square degrees, while $\beta_{\rm field}$ describes the scaling of the number of false detections with ξ as defined in Equation (3). $\gamma_{\rm field}$ describes the renormalization of $A_{\rm SZ}$ in the SZ–mass scaling relation of Equation (2).

Two-dimensional maps of the sky are made by binning the time-ordered data (TOD), to which mild time-domain filtering has been applied, into 0.25 arcmin pixels. This produces estimates of the 95 and 150 GHz sky, to which we apply a simultaneous spatial-spectral filter, yielding a filtered estimate of the tSZ sky, optimized for extracting cluster candidates. The candidates are identified using a peak-finding algorithm.

Due to the exact choice of field extent, as well as the finite footprint of the SPT-SZ array on the sky, the fields overlap slightly. The overlap regions only comprise $\sim$2% of the total survey area, and for simplicity we choose to treat the fields as fully independent. As a result of this treatment, we would expect to double-count roughly 2% of cluster candidates, or seven to eight of our total number of candidates. In fact we find nine cases of candidates with a very high probability of having been detected in two different fields (i.e., 18 total candidates that correspond to nine physical clusters). There is no bias to our cosmological constraints from this treatment. Our uncertainties will be very slightly underestimated, but this has a negligible effect on our final cosmological constraints.

2.1.1. SZ–Mass Scaling Relation Parameterization

We use the same functional form for the SZ–mass scaling relation as previous SPT cluster cosmology analyses (V10; Benson et al. 2013; hereafter B13; Reichardt et al. 2013; hereafter R13; Bocquet et al. 2015).

Briefly, we introduce two SZ parameters related to the cluster detection process. The first is the detection significance ξ. After generating filtered synthesized SZ maps at a series of filter scales, each map pixel value is divided by the rms of the map in a strip that spans 90 arcmin in declination. Then the maximum peak height over all filter scales is identified and defined as ξ, the SZ observable used in this paper. Because this observable allows for a very well understood selection function, and cosmological constraints are dominated by the unknown normalization of the observable-mass scaling relation, we find that this observable is preferred over going to a different SZ observable such as $Y_{\rm SZ}$.

The second parameter is the unbiased significance ζ. It is defined as the value of ξ that would be found in the absence of instrumental noise and astrophysical contaminants (including the SZ background). Due to the fact that ξ is determined by maximizing the significance after searching in two-dimensional position space and source template size, the average ξ found across many noise realizations is enhanced by those three degrees of freedom, resulting in the approximate relation

$$\langle \xi \rangle^2 = \zeta^2 + 3. \quad (1)$$

Since this relation cannot hold down to very low ζ, we only model this maximization bias for $\zeta > 2$. We find that changing the location of this cutoff to $\zeta > 1.5$ or $\zeta > 2.5$ has negligible impact on the results presented in this work. Motivated by the definition of ξ, and the fact that the astrophysical contaminants and instrument noise are Gaussian to a high degree, we model ξ as related to $\langle \xi \rangle$ by unit-width Gaussian scatter. We then parameterize the ζ–M scaling relation as

$$\zeta = A_{\rm SZ}\left(\frac{M}{3 \times 10^{14} M_{\odot} h^{-1}}\right)^{B_{\rm SZ}}\left(\frac{E(z)}{E(0.6)}\right)^{C_{\rm SZ}}, \quad (2)$$

with an additional log-normal intrinsic scatter parameter $\sigma_{\ln \zeta}$. The dimensionless Hubble parameter is denoted by $E(z)$. We follow B13 and R13 and apply Gaussian priors to these scaling relation parameters. However, the mean values and widths of the priors are updated to reflect results from the more recent cosmo-OWLS hydrodynamic simulations (Le Brun et al. 2014), which will be discussed in Section 2.2. Specifically, we use the Gaussian priors $A_{\rm SZ} = 5.38 \pm 1.61$, $B_{\rm SZ} = 1.340 \pm 0.268$, $C_{\rm SZ} = 0.49 \pm 0.49$, and $\sigma_{\ln \zeta} = 0.13 \pm 0.13$, while requiring $\sigma_{\ln \zeta} > 0.05$.

2.2. By-field Simulations

Each of the 19 fields that comprises the 2500 square degree survey has slightly different properties, which we account for using two similar types of simulations. The first is to account for the fact that the map noise is slightly different in each of the fields. This causes the detection significance ξ (the selection observable) of a cluster to relate to true underlying mass differently depending on the field in which the cluster was found. We model this by simulating the relation between true cluster mass and unbiased significance ζ separately for each field. The simulations contain several components.

1. A Gaussian random field with a power spectrum equal to the CMB power spectrum calculated using the best-fit ΛCDM parameters from Keisler et al. (2011).
2. A Gaussian random field meant to approximate the background of emissive point sources after the brightest sources are masked. The power spectrum is generated using three components. The first is a Poisson component modeling the radio point source population with an amplitude at $\ell = 3000$ of $D^r_{3000} = 1.28 \mu {\rm K_{CMB}}^2$ at 150 GHz and spectral index $\alpha_r = -0.6$ (defined by flux $\propto \nu^{\alpha}$). The second and third components model the Poisson and clustered dusty star-forming galaxy (DSFG) populations, respectively. The assumed spectral index is $\alpha_{\rm DSFG} = 3.6$ and the amplitudes are the best-fit values from Shirokoff et al. (2011).
3. Atmospheric and instrumental noise. These are simulated using the actual TOD. The coherent nature of the sky signal, modulated by the scan strategy, and the incoherent nature of the instrumental and atmospheric noise contributions allow us to estimate the map noise by simply subtracting the right-going scan TOD from the left-going scan TOD (up- and down-going in the case of most of the ra21hdec-50 field) in the map-making process. This removes any coherent signal present on the sky. We furthermore apply a sign change to half the observations before they are coadded into the final map. By changing which signs are assigned, we generate different realizations of realistic noise maps.
4. Maps of the Compton y parameter from the cosmo-OWLS simulations in Le Brun et al. (2014). We use maps from the AGN8.0 model and convert the Comptonization maps to CMB temperature units by integrating the measured frequency response of the instrument against a relativistic 5 keV tSZ spectrum.

A modified version of the standard cluster-finding process is run on the sum of these four components, and the cluster candidates are recorded. In addition, the same spatial-spectral filter is applied to the maps only containing SZ signal. The latter is used to identify cluster candidates and define their SZ center. The amplitude in these filtered, SZ-only maps, divided by the standard deviation in a 90 arcmin strip in the filtered maps that include noise, is precisely the unbiased significance ζ introduced in Section 2.1.1. These candidates are then compared to the underlying halo catalog used to generate the mock SZ maps, which provide the cluster redshift. For each SZ-identified cluster candidate, we choose the nearest dark matter halo with $M_{200} > 5 \times 10^{13} M_{\odot}$.

With mass, unbiased significance and redshift in hand, we use the method of least absolute deviations to fit the ζ–M relation from Equation (2) over the range $z > 0.25$, $M_{500} > 1 \times 10^{14} M_{\odot}$. We find nearly identical results when using a linear least-squares method. The normalization parameter $A_{\rm SZ}$ differs from field to field by up to 30%, while the other scaling relation parameters only vary at the few percent level. We therefore model field variation with one parameter $\gamma_{\rm field}$ that renormalizes the overall scaling: $A_{\rm SZ} \rightarrow \gamma_{\rm field} A_{\rm SZ}$. For consistency with previous publications, we normalize $\gamma_{\rm field}$ so that the weighted average over the three fields which share 100% of the raw data used in R13 matches

the weighted average in that work. We note that any other choice of normalization would simply alter the definition of $A_{\rm SZ}$, leaving all other results unaffected. The values of $\gamma_{\rm field}$ are shown in Table 1.

The other field-specific simulation is used to compute the expected false detection rate. At a detection threshold of $\xi > 5$, approximately 5% of cluster candidates are expected to be false. In order to simulate the rate of false detections, we perform the cluster-finding process on the simulated maps described above, omitting the SZ component. The resulting number of cluster candidates as a function of ξ is recorded for 100 such simulations. To reduce shot noise from the finite number of simulated realizations, we model the false detection rate with the empirically chosen fitting function

$$N_{\rm false}(>\xi) = \alpha_{\rm field} \exp(-\beta_{\rm field}(\xi - 5)). \quad (3)$$

The values of $\alpha_{\rm field}$ and $\beta_{\rm field}$ are shown in Table 1. The total number of expected false detections per 2500 square degrees with $\xi > 5$ from these simulations is 18 ± 4, which is consistent with the number of optically unconfirmed cluster candidates, 21 (B15).

3. REDSHIFT ESTIMATION

As the SPT-SZ selection is essentially independent of redshift, we require optical and—for the highest-redshift systems—near-infrared (NIR) data to both confirm the SPT candidates as clusters and to obtain redshifts for these systems. We provide a brief overview of this process here; for more details readers are referred to B15.

As a first step, each SPT cluster candidate is visually inspected in imaging data from the Digitized Sky Survey (DSS),[49] as we have found most SPT clusters at redshift $z < 0.5$ are visible in these scanned photographic plates. These relatively low-redshift systems are then reimaged with 1–2 m class telescopes to obtain robust confirmations and redshifts. Higher-redshift candidates not visible in the DSS (or designated non-confirmed after imaging on the small telescopes) are observed with 4–6.5 m class telescopes. The latter observations are conducted in two passes: first-pass observations are designed to ensure $\geqslant 5\sigma$ detection of $0.4L^*$ red-sequence galaxies (where L^* is the characteristic luminosity that appears in the Schechter 1976 formulation of the galaxy luminosity function) at $z < 0.75$; higher-redshift clusters or candidates not confirmed in the first pass are also observed (telescope resources permitting) in the optical and/or NIR to extend this redshift range to $z > 0.9$. In total 69/78 of the highest-redshift ($z > 0.75$) or non-confirmed systems received second-pass imaging; the majority of these systems (58/78) were observed with *Spitzer*/IRAC (Fazio et al. 2004, PI: Brodwin) at 3.6 μm and 4.5 μm to a depth sufficient for the 10σ detection of $0.4L^*$ galaxies at $z = 1.5$ (Brodwin et al. 2010).

Following imaging, a few arcmin region around each SPT location is searched for an overdensity of red-sequence cluster galaxies. When such an overdensity is identified, we confirm the candidate as a cluster and assign the system a redshift using a red-sequence model calibrated using the subset of SPT clusters with spectroscopic redshifts. For candidates not confirmed in our imaging data we compute a redshift "lower limit" corresponding to the highest redshift for which we would have detected the overdensity of red galaxies we require to confirm a cluster (Song et al. 2012). The redshift range of the confirmed cosmological cluster sample is $0.25 \leqslant z \lesssim 1.7$ with a median redshift $z_{\rm med} = 0.58$. Typical redshift uncertainties range from $\sigma_z \sim 0.02 \times (1+z)$ for the optical-based redshifts to $\sim 0.035 \times (1+z)$ for clusters with redshifts determined from *Spitzer*/IRAC observations.

A large subset (31%) of the SPT cosmological cluster sample has also been spectroscopically observed. Spectroscopic redshifts for 86 SPT clusters were obtained as part of a dedicated follow-up campaign using spectrographs on the Magellan telescope, the Gemini-South telescope, and the Very Large Telescope. We have also searched the literature for cluster counterparts and find an additional 21 clusters with reported spectroscopic redshifts. The spectroscopic sample spans almost the full redshift range of the cluster sample, from $0.26 < z \leqslant 1.478$, with a median redshift of $z_{\rm med} = 0.53$. The SPT spectroscopic follow-up effort is described in detail in Ruel et al. (2014), and the redshifts are presented in B15.

4. *CHANDRA* X-RAY DATA SET AND METHODS

The X-ray data used in this work were originally presented in McDonald et al. (2013b) and most were acquired as part of a *Chandra* X-ray Visionary Project (PI: Benson). In general, exposure times were chosen to ensure 2000 X-ray counts, based on measured *ROSAT* fluxes (when available) or a combination of the $L_{\rm X}$–M relation and mass estimates from the SZ signal. Data were obtained using the front-illuminated ACIS-I CCDs, and cleaned for background flares before applying calibration corrections using CIAO v4.7 and CALDB v4.6.8.

Global cluster properties (e.g., gas mass $M_{g,500}$ and X-ray temperature kT_{500}) for each cluster are derived in McDonald et al. (2013b), following closely the procedures described in Andersson et al. (2011). For a detailed description of the X-ray analysis, the reader is directed to these works. Here, we make use of the mass proxy $Y_{\rm X}$, which is obtained from the measured gas mass and X-ray temperature. This temperature kT_{500} is derived by first assuming some value of r_{500} (i.e., 1 Mpc), and measuring the core-excised ($0.15\,r_{500}$ to $1.0\,r_{500}$) temperature within this radius. Using this temperature, we compute a new estimate of r_{500} using the $T_{\rm X}$–M relation from V09. The temperature is then measured within this radius, and the process is repeated until it converges.

We also measure the enclosed gas mass as a function of r_{500}, following the procedures described in McDonald et al. (2013a). This involves measuring the X-ray surface brightness in the rest-frame energy range 0.7–2.0 keV as a function of radius, and fitting a line-of-sight projected model for the electron density profile to these data, following Vikhlinin et al. (2006). In converting from the electron density to the gas density, we assume $\rho_g = m_p n_e A/Z$, where $A = 1.397$ is the average nuclear charge and $Z = 1.199$ is the average nuclear mass. The enclosed gas mass within a given radius is simply the volume integral of the gas density profile out to the specified radius.

These two quantities are combined into the mass proxy $Y_{\rm X}$. Since r_{500} must be known to compute $M_{g,500}$, we numerically solve $Y_{\rm X} = M_{g,500} kT_{500}$ together with the scaling relation given in Equation (4). This numerical calculation is performed for each set of cosmological parameters that will be explored in Section 5.

[49] http://archive.stsci.edu/dss/

4.1. Y_X–M Scaling Relation Parameterization

Following V09, B13, R13, and Bocquet et al. (2015), we use Y_X as a proxy for the total cluster mass. We write the scaling relation as

$$\frac{M_{500}}{10^{14}M_\odot/h} = \left(A_X h^{3/2}\left(\frac{h}{0.72}\right)^{\frac{5}{2}B_X-\frac{3}{2}}\right) \times \left(\frac{Y_X}{3\times 10^{14}M_\odot \text{ keV}}\right)^{B_X} E(z)^{C_X}, \quad (4)$$

where the parameters A_X, B_X, C_X describe the normalization, mass dependence and redshift dependence of the relation, respectively.[50] As we did for the ζ–M relation, we introduce a parameter $\sigma_{\ln Y_X}$ which models a log-normal intrinsic scatter in the Y_X–M relation. We allow the intrinsic scatter in the Y_X–M relation and the ζ–M relation to be correlated, parameterizing this with the correlation coefficient ρ_{ζ,Y_X}. We follow B13 and R13 and apply Gaussian priors of $B_X = 0.57 \pm 0.03$, $C_X = -0.40 \pm 0.20$, and $\sigma_{\ln Y_X} = 0.12 \pm 0.08$, respectively, as well as a uniform prior between -0.98 and 0.98 on ρ_{ζ,Y_X}.

4.2. Prior on the Normalization of the Y_X–M Relation

In B13 and R13, we used a prior on the normalization of the Y_X–M relation, A_X, motivated from V09. In V09, the normalization was cross-checked against WL mass estimates from Hoekstra (2007) for the 10 clusters at $z < 0.3$ that, at the time, also had sufficient *Chandra* observations to measure Y_X. In B13, this normalization was remeasured using more recent WL mass estimates from Hoekstra et al. (2012), and found to be consistent with the assumed calibration from V09. In this work, we revisit the Y_X–M normalization, using the most recent WL mass estimates from H15 to constrain any mean offset in the normalization of the original hydrostatic mass calibration of the Y_X-mass scaling relation from V09. In addition, we also consider any systematic offset in the H15 WL mass estimates, by comparing to alternative WL mass estimates from WtG.

In Figure 1, we compare WL-based mass estimates from H15 to Y_X-based mass estimates and to weak-lensing masses from WtG. We have remeasured Y_X from archival *Chandra* X-ray data for the 14 clusters from H15 with sufficiently deep X-ray measurements, which we use to estimate a cluster mass (M_{Y_X}) using the Y_X-mass scaling relation from V09. For these clusters, we also remeasure the deprojected weak-lensing aperture mass from the H15 data set using the X-ray implied r_{500}. Using the X-ray implied r_{500} approximates what would happen if the WL mass estimates were included in a joint Y_X–WL scaling relation fit because of the relatively low scatter of Y_X with cluster mass and, as we will show later, the agreement in the resulting Y_X–M relation. To compare H15 and WtG mass estimates at the same radius, we extract a WtG mass for each of the 18 clusters in common at the value of r_{500} implied by the H15 analysis. We specifically use the mass estimates computed by fitting an NFW model to the observed shear profiles from the WtG "color-cut" method (Applegate et al. 2014).

In Table 2, we give three different measures of the relative cluster mass estimates between H15, WtG, and V09. First, we fit a scaling relation of the form $\ln(M_{WL}) = A + \ln(M_{Y_X})$ with a free log-normal intrinsic scatter, using the Bayesian linear regression fitting code from Kelly (2007). For comparison, we also estimate the bootstrap mean and median of the log of the mass ratio, which makes no assumption about the underlying scatter.

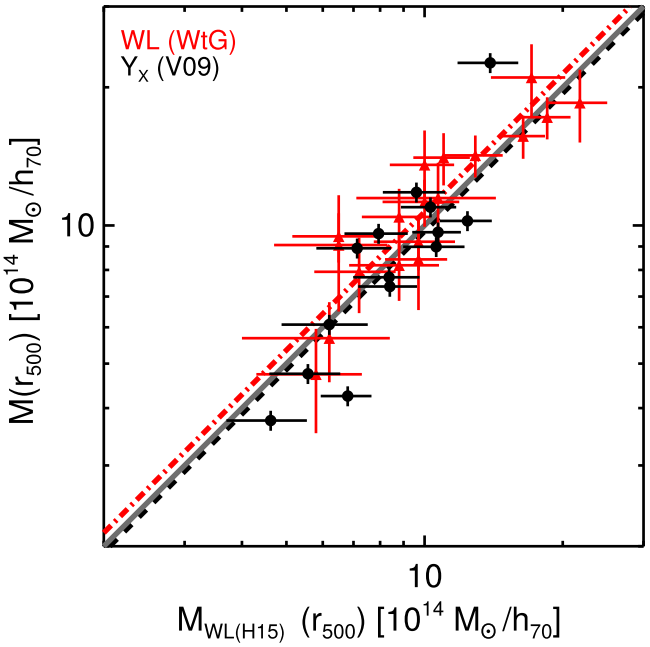

Figure 1. A plot comparing cluster weak lensing and Y_X-based mass estimates. Plotted along the y-axis are weak lensing-based mass estimates from WtG (red) and Y_X-based mass estimates using the scaling from V09 (black). On the x-axis are weak lensing-based mass estimates from H15. For the H15/V09 comparison (black points), we have re-estimated the H15 masses using the X-ray implied r_{500}. The solid grey line shows a one-to-one relation, and the dashed black and red lines give the normalization implied for the bootstrap mean fit to the ratio of the masses (for details see text).

Table 2
Mass Ratios between Weak Lensing (H15, WtG) and Y_X (V09) Based Mass Estimates

Data set	N_{clust}	Log-normal	Mean	Median
H15/V09	14	1.01 ± 0.07	1.03 ± 0.06	1.12 ± 0.05
WtG/H15	18	1.06 ± 0.07	1.07 ± 0.07	1.11 ± 0.05
WtG/V09	8	1.15 ± 0.10	1.17 ± 0.13	1.24 ± 0.09

First considering the mass ratio between H15 and V09, we find all three estimates imply a mass ratio near unity with the scaling relation, bootstrap mean, and bootstrap median, giving ratios of 1.01 ± 0.07, 1.03 ± 0.06, and 1.12 ± 0.05, respectively. This implies that the Y_X-based masses from V09 are in relatively good agreement with H15, with the H15 masses ~1%–12% larger, depending on how the mass ratio is estimated. Next, we consider the mass ratio between WtG and H15. We also find that all three estimates imply a mass ratio near unity with the scaling relation, bootstrap mean, and bootstrap median giving ratios of 1.06 ± 0.07, 1.07 ± 0.07, and 1.11 ± 0.05, respectively. Therefore the WL-based mass estimates from H15 and WtG are also in relatively good agreement, with the WtG masses ~6%–11% larger, comparable to the 7% estimated systematic uncertainty from H15. The overlapping cluster sample between our V09-Y_X sample and WtG is smaller (eight clusters), and therefore has larger

[50] This equation differs slightly from B13 and R13 in order to more rigorously scale the V09 results if $B_X \neq 0.6$ and $h \neq 0.72$ simultaneously. This modification has a negligible effect on any of the results in this work.

uncertainty on the mass ratio. We find that the three different mass ratio estimates between WtG and V09 range from 1.15–1.24. This range is somewhat larger than, but comparable with, the expectation when considering the mass ratios of the larger samples used to calculate the WtG/H15 and H15/V09 mass ratios, which would predict a mass ratio between WtG and V09 of ∼1.1–1.2.

In summary, comparing to the original Y_X–M calibration from V09, we find that the WL measurements imply a normalization that increases the Y_X-based cluster masses by a factor between 1.0 and 1.2, depending on the WL analysis and data set (H15, WtG), and the fit assumptions. We therefore choose a Gaussian prior on the normalization of our Y_X–M relation of $A_X = 6.35 \pm 0.61$, which increases the normalization from V09 by a factor of 1.1 with an overall uncertainty of 10%. We expect that this uncertainty includes the sum of our statistical and systematic uncertainty, because it brackets the range of values in the above comparison with the WL measurements and is comparable to our naive expectation given the statistical uncertainty in the fit above and the systematic uncertainty estimated in H15. This effectively gives us a purely WL-derived mass scale, independent of the hydrostatic mass estimates. We expect our constraints on the mass scale to improve in future work using WL observations of SPT-SZ survey clusters, which we will then be able to directly include in our cosmological analysis.

Finally, we have also estimated the dependence of the weak-lensing and X-ray-derived mass estimates on cosmological parameters. Over the range of cosmological parameters explored, the ratio of the two varies negligibly compared to the uncertainty of 10%.

5. COSMOLOGICAL ANALYSIS

Armed with the abundance of clusters as a function of the observables z, ξ, and Y_X, and models of the scaling of these observables with cluster mass, we are almost ready to place constraints on the cosmological parameters. For the final step, we need a theoretical framework for translating the cosmological parameters into a prediction for the number of clusters as a function of mass and redshift, and we need a statistical method for comparing those predictions to our observed abundance. For both of these requirements, we closely follow the methods of V10, B13, and R13.

5.1. Parameters to Cluster Abundance Predictions

For a given set of cosmological parameters, we use the Code for Anisotropies in the Microwave Background (CAMB, Lewis et al. 2000) to generate the matter power spectrum as a function of redshift. We use this power spectrum as input to the Tinker et al. (2008) halo mass function, with which we calculate the number of dark matter halos as a function of spherical overdensity mass M_{500} and redshift.

More recent results (e.g., Bhattacharya et al. 2011; Skillman et al. 2014) confirm that, over the range of cluster masses and redshifts considered in this work, the Tinker mass function is accurate to a level that is more than sufficient for the cosmological parameter constraints presented. For instance, even a shift as large as 10% in the halo mass function at $M_{500} \sim 3 \times 10^{14}\, M_\odot$ would only affect the cosmological constraints presented in Section 6.2 at the $\lesssim 0.2\sigma$ level.

Given the Tinker mass function, we relate the cluster mass to the observed quantities ξ and Y_X using the scaling relations described in Sections 2.1.1 and 4.1.

In our default cosmological analysis, we use the standard six-parameter ΛCDM model, parameterized by the physical densities of baryons and cold dark matter at $z = 0$, $\Omega_b h^2$ and $\Omega_c h^2$, the angular scale of the sound horizon at last scattering θ_s, the tilt of the scalar power spectrum n_s, the amplitude of the scalar power spectrum A_s, and the optical depth to reionization τ. We will often refer to values of parameters derived from combinations of these original six, such as σ_8, the amplitude of linear matter fluctuations on 8 Mpc/h scales at $z = 0$, Ω_m, the total matter density at $z = 0$, and $H_0 = 100h$ km s^{-1} Mpc^{-1}, the value of the Hubble parameter at $z = 0$. We explore three extensions to ΛCDM. We first explore a model in which the sum of the neutrino masses Σm_ν is a free parameter. In this work we use the prescription from Costanzi et al. (2013) to predict the effect of massive neutrinos on the halo mass function. We also consider a cosmological model in which Σm_ν and $N_{\rm eff}$, the effective number of relativistic particle species, are both free parameters, and a model in which w, the parameter describing the equation of state of dark energy, is allowed to vary.

5.2. Cluster Likelihood Evaluation

To compare theoretical predictions for cluster abundance to the observations in this work, we closely follow the likelihood derivation of V10, B13, and R13. We differ from those analyses in this work by presenting an efficient numerical technique that scales linearly rather than exponentially with the number of mass proxies.

As is appropriate for a cluster abundance measurement (Hu & Kravtsov 2003; Holder 2006), we start with the binned Poisson statistic in cluster observable space, which consists of redshift z and an arbirary number of mass proxies. In this work, we use the SZ mass proxy ξ which was described in Section 2.1.1, and the X-ray mass proxy Y_X as described in Section 4.1. For a given observable-space bin x_i, the probability of observing n events, with expectation value $y(x_i)$ is

$$P_i = \frac{e^{-y(x_i)} y(x_i)^n}{n!}. \tag{5}$$

We choose to take the limit of small bins where y becomes arbitrarily small at all x_i, and n is zero except at the locations of x_i where clusters have been observed (Mantz et al. 2008, 2010, V09). If we let x_j denote the bin that contains the jth cluster, we obtain

$$\ln \mathcal{L} = \sum_i \ln P_i = -\sum_i y(x_i) + \sum_j \ln y(x_j), \tag{6}$$

where i runs over all observable space bins, and j runs over detected clusters. In this work, we are dealing specifically with the three-dimensional cluster observable space $\{z, \xi, Y_X\}$, so we can write the model expectation value $y(x_i) = N(z_i, \xi_i, Y_{X,i})$ and express the likelihood as

$$\ln \mathcal{L} = -\sum_{i_1,i_2,i_3} N(z_{i_1}, \xi_{i_2}, Y_{X,i_3}) + \sum_j \ln N(z_j, \xi_j, Y_{X,j}), \tag{7}$$

where the i_1, i_2, i_3 sums again run over all possible values and j only runs over the bins where clusters were detected. Going to the continuous limit would result in a divergent likelihood expression. This can be understood by the fact that the model is increasingly unlikely to produce our particular realization of the cluster catalog as we go to finer binning. The divergence can be removed by simply adding $-\ln \Delta z \Delta\xi \Delta Y_{\rm X}$ to Equation (7). This quantity (the logarithm of the observable-space bin volume) depends only on the choice of bin size, so that $\Delta \ln \mathcal{L}$ for different values of cosmological or scaling relation parameters remains meaningful. This procedure corresponds to substituting the number density $dN(z, \xi, Y_{\rm X})/dzd\xi dY_{\rm X}$ for the number contained in a bin $N(z_j, \xi_j, Y_{{\rm X},j})$. We then obtain the expression

$$\ln \mathcal{L} = -\int dzd\xi dY_{\rm X} \frac{dN(z, \xi, Y_{\rm X})}{dzd\xi dY_{\rm X}} + \sum_j \ln \frac{dN(z_j, \xi_j, Y_{{\rm X},j})}{dzd\xi dY_{\rm X}}. \quad (8)$$

V10, B13, and R13 evaluated this expression on either a two-dimensional or three-dimensional uniformly spaced grid. Each dimension was gridded into several hundred points, so that the computational cost rises exponentially with the number of mass proxies. The computational cost was trivial for V10, challenging for B13 and R13, and likely intractable in future work if another mass proxy is added. The techniques used in Mantz et al. (2010) and Vikhlinin et al. (2009b) also scale exponentially with the number of mass proxies.

Instead of computing Equation (8) on a uniformly spaced grid, we use the following numerical techniques. First, we note that the follow-up mass proxy $Y_{\rm X}$ immediately integrates out of the first term. This applies to any mass proxy that does not appear in the survey selection function. Therefore, we only need to perform a two-dimensional integral

$$-\int dzd\xi dY_{\rm X} \frac{dN(z, \xi, Y_{\rm X})}{dzd\xi dY_{\rm X}} = -\int_{z_{\rm cut}}^{\infty} dz \int_{\xi_{\rm cut}}^{\infty} d\xi \frac{dN}{dzd\xi}. \quad (9)$$

We evaluate this expression with

$$\int_{z_{\rm cut}}^{\infty} dz \int_{\xi_{\rm cut}}^{\infty} d\xi \frac{dN}{dzd\xi} = \int_{z_{\rm cut}}^{\infty} dz \int_0^{\infty} dM \frac{dN}{dzdM} P(\xi > \xi_{\rm cut}|M), \quad (10)$$

where $P(\xi > \xi_{\rm cut}|M)$ is simply the significance cut modeled through the scaling relation as described in Section 2.1.1.

The second term of Equation (8) is more challenging to evaluate. It can be written as an integral over the mass function,

$$\frac{dN(z_j, \xi_j, Y_{{\rm X},j})}{dzd\xi dY_{\rm X}} = \int dz' d\langle\xi\rangle dY_{{\rm X}'} d\ln M \times P(z_j|z') P(\xi_j|\langle\xi\rangle) P(Y_{{\rm X},j}|Y_{{\rm X}'}) \times P(z', \langle\xi\rangle, Y_{{\rm X}'}|z, \ln M) \frac{dN}{dzd\ln M}. \quad (11)$$

The probability density functions $P(z_j|z')$, $P(\xi_j|\langle\xi\rangle)$, and $P(Y_{{\rm X},j}|Y_{{\rm X}'})$ describe the (independent) measurement error of each of the observables. $P(z', \langle\xi\rangle, Y_{{\rm X}'}|z, \ln M)$ describes the joint scaling relations, implemented with multi-dimensional log-normal intrinsic scatter. In our case of two mass proxies (ξ, $Y_{\rm X}$), this is implemented with three parameters: two describing the marginal variances $\sigma_{\ln\zeta}$ and $\sigma_{Y{\rm X}}$, as well as one correlation coefficient $\rho_{\zeta,Y{\rm X}}$, each of which is marginalized over in this work. Due to the treatment of maximization bias in Section 2.1.1, the scaling relation is defined in terms of ζ rather than $\langle\xi\rangle$. We perform the change of variables using

$$P(z', \langle\xi\rangle, Y{\rm X}'|z, \ln M) = \int d\zeta' \frac{1}{\zeta'} \exp\left(-\frac{1}{2}(\langle\xi\rangle - \zeta')^2\right) P(z', \zeta', Y{\rm X}'|z, \ln M). \quad (12)$$

The computational bottleneck for evaluating the cluster likelihood lies in evaluating Equation (11). We use Monte Carlo integration, randomly drawing from the probability distribution $P(z_j|z')$ $P(\xi_j|\langle\xi\rangle)$ $P(Y_{{\rm X},j}|Y{\rm X}')$ $P(z', \langle\xi\rangle, Y{\rm X}'|z, \ln M)$, weighted by the mass function $\frac{dN}{d\ln M}$. Let $\ln m_k'$ denote the kth integration variable corresponding to its flat-prior mass estimate (i.e., ζ' and $Y{\rm X}'$ substituted into their respective observable-mass scaling relations). We can then write

$$P(\ln m_k'|\ln M') = \frac{1}{\sqrt{(2\pi)^{N_{\rm obs}}|\Psi|}} \exp\left(-\frac{1}{2}\sum_l (\ln m_k' - \ln M')(\Psi^{-1})_{kl}(\ln m_l' - \ln M')\right), \quad (13)$$

where Ψ is the mass proxy covariance matrix containing the intrinsic scatter and correlation coefficient parameters introduced in Sections 2.1.1 and 4.1 so that $\Psi_{kl} = \langle(\ln m_k' - \ln M')(\ln m_l' - \ln M')\rangle$.

Now, we wish to obtain samples of the integration variable $\ln M'$, given the location at which we are attempting to evaluate $dN(x_j)/dx$. In order to efficiently draw samples we first, for each k, draw samples from the (inverse) measurement error $P(x_{k,j}|x_k')$, which is assumed to be independent for each k. We then substitute these values into the scaling relations to obtain an ensemble of $\ln m_k'$ values. The remaining task is then to draw random deviates $\ln M'$ that follow the probability distribution explicitly shown in Equation (13), given each value of $\ln m_k'$. To do so, we note that

$$\begin{aligned}\Sigma_{kl}(\ln m_k' - \ln M')(\ln m_l' - \ln M')(\Psi^{-1})_{kl} &= \Sigma_{kl} \ln m_k' \ln m_l' (\Psi^{-1})_{kl} - 2\ln M' \Sigma_k \ln m_k' \Sigma_l (\Psi^{-1})_{kl} + \ln M'^2 \Sigma_{kl}(\Psi^{-1})_{kl} \\ &= T_0 - 2T_1 \ln M' + T_2 \ln M'^2 \\ &= \left(\frac{\ln M' - T_1/T_2}{1/\sqrt{T_2}}\right)^2 + T_0 - \frac{T_1^2}{T_2}, \end{aligned} \quad (14)$$

where $T_0 = \Sigma_{kl} \ln m_k' \ln m_l' (\Psi^{-1})_{kl}$, $T_1 = \Sigma_k \ln m_k' \Sigma_l (\Psi^{-1})_{kl}$, and $T_2 = \Sigma_{kl}(\Psi^{-1})_{kl}$, which is quadratic in $\ln M'$, so that Equation (13) is a log-normal distribution in M' with a known mean, width and normalization. We compute T_0, T_1, and T_2 explicitly and sample from the resulting distribution.

Having obtained samples of $\ln M'$, which we denote as $\ln \tilde{M}'$, we average the mass function

$$\frac{1}{N_{\rm samples}} \sum_i \frac{dN}{d\ln M'}\Big|_{\ln \tilde{M}'_i} \sqrt{\frac{T_2}{2\pi}} \frac{\exp -\frac{1}{2}\left(T_0 - \frac{T_1^2}{T_2}\right)}{\sqrt{(2\pi)^{N_{\rm obs}}|\Psi|}} \quad (15)$$

and combine with Equation (14) to obtain an estimate for Equation (11). Our implementation of this estimator has been demonstrated to be unbiased through extensive simulations, with well-behaved residuals. The error on the mean is found to decrease as the inverse square root of the number of deviates drawn. In practice, for two mass proxies and 377 cluster candidates, we draw 10^4 deviates per cluster candidate, resulting in rms noise on the likelihood surface of $\Delta(-2\ln\mathcal{L}) \lesssim 0.1$ near the maximum likelihood. For the cluster catalog used in this work, the execution time is approximately one second on a single CPU thread. This likelihood module has been checked against an independent implementation, based on the estimator presented in Bocquet et al. (2015). The comparison shows agreement to well within the 1σ uncertainties on the cosmological parameter constraints found in this work.

5.3. External Data sets

In Section 6, we will discuss the cosmological constraints obtained using the analysis laid out so far. We will evaluate the compatibility of the cluster data with other data sets, as well as show the improvements in parameter constraints when the cluster data set is combined with other data sets. The primary external data we use are CMB power spectrum measurements, measurements of BAO from galaxy surveys, and distances to Type Ia supernovae (SNe).

The canonical CMB power spectrum data we use is the temperature–temperature power spectrum from the *Planck* 2013 release, combined with low-ℓ polarization information from *WMAP* (Planck Collaboration et al. 2014a, hereafter *Planck*+WP). The qualitative results from this work will be very similar to those that would have been obtained by considering the *Planck* 2015 data set, since the constraints on σ_8 and Ω_m from the temperature and low-ℓ polarization power spectrum are very similar between the two *Planck* releases. In Section 6.2, we will briefly review the effect of substituting the best CMB power spectrum data from before the *Planck* 2013 release, using instead the combination of *WMAP*9 (Hinshaw et al. 2013) and SPT (Story et al. 2013, hereafter S13) CMB power spectrum data.

We sometimes use a prior on the angular scale of the sound horizon θ_s. This is a powerful piece of cosmological information, and relies only very weakly on the details of the CMB analysis, since it affects the peak positions. We use the *Planck*+WP measurement, though we conservatively increase the uncertainty by a factor of five to $100\theta_{\rm MC} = 1.0413 \pm 0.0034$.[51] Since θ_s is so well-measured, none of the results presented in this work that use a prior on θ_s are sensitive to the specific value of the assumed uncertainty.

When BAO data are used in this work, we use the SDSS-III BOSS results from data release 11. Specifically, we use the measurements of the parameter combination D_V/r_s at $z = 0.32$ (LOWZ) and $z = 0.57$ (CMASS) from Anderson et al. (2014).

When considering cosmologies with a free parameter describing the dark energy equation of state, we compare to and contrast with the SN results from the joint likelihood analysis of the SDSS-II and SNLS SN samples from Betoule et al. (2014).

Cluster abundances do weakly constrain the baryon density, but for our main results we choose to adopt a prior based on big-bang nucleosynthesis calculations and deuterium abundance measurements of $\Omega_b h^2 = 0.02202 \pm 0.00045$ (Cooke et al. 2014). Rather than fixing this parameter, we marginalize over the uncertainty, though that analysis choice has no significant effect on the results presented in this work.

Finally, where stated, we adopt a prior of $H_0 = 73.8 \pm 2.4\ {\rm km\ s^{-1}\ Mpc^{-1}}$ from the direct H_0 measurements of Riess et al. (2011). We find that changing this prior by 1σ affects the resulting σ_8 constraint by $\lesssim 0.2\sigma$, while the Ω_m constraint is affected by $\sim 0.4\sigma$. These two effects are anti-correlated so that the commonly used parameter combination $\sigma_8 (\Omega_m/0.27)^{0.3}$ is highly insensitive to the assumed value of H_0.

6. COSMOLOGICAL CONSTRAINTS

In this section, we discuss the parameter constraints obtained using the data and methods described in the previous sections. We first explain which parameters and combinations of parameters are most strongly constrained by cluster abundance measurements. We then discuss the constraints from this cluster sample, both in comparison to and in combination with other cosmological data sets, for different choices of cosmological models. We assume spatial flatness throughout this work.

6.1. Parameter Sensitivity to Cluster Abundance

A measurement of cluster abundance as a function of redshift provides constraints on cosmological parameters through several mechanisms. First, the total number of clusters found strongly depends on the matter density and the amplitude of the matter power spectrum (e.g., Bahcall & Cen 1992; White et al. 1993). As shown in, e.g., White et al. (1993), a simple spherical-collapse model for the halo mass function (Press & Schechter 1974) indicates that the total number of clusters should most strongly constrain the parameter combination $\sigma_8 \Omega_m^\alpha$, where α is related to the local slope of the matter power spectrum at the mean mass of the cluster catalog. This prediction has been empirically borne out in many cluster abundance studies, including this one.

The redshift dependence of the cluster abundance contains information on the growth function, as well as a dependence on the cosmic volume surveyed. This combination of sensitivity to growth and volume provides a unique constraint on parameters that affect the expansion history, notably w, the equation of state of dark energy (e.g., Haiman et al. 2001). In the case of w, the effect of changing this parameter on the cluster abundance actually changes sign at $z \sim 1$ (e.g., Figure 1 of Mohr 2005). The 377 cluster candidates presented in this work provide a large enough sample to constrain cosmological parameters by measuring the evolution of cluster abundance. However, this constraint is also potentially limited by knowledge of the observable-mass scaling relations, in this case their evolution

[51] $\theta_{\rm MC}$ is the approximation to θ_s used in CosmoMC (Lewis & Bridle 2002).

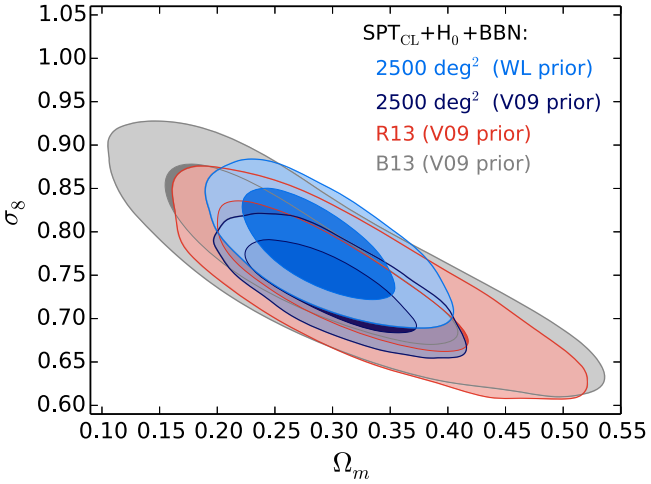

Figure 2. Comparison of cluster constraints on σ_8 and Ω_m from this work with those from previous SPT publications. The B13 analysis (outermost, gray contours) used 18 clusters, 14 of which have *Chandra* observations. The number of clusters increased to 100 in R13 (red contours), whereas this work uses 377 cluster candidates, 82 of which have high-quality *Chandra* observations. If we adopt the same observable-mass priors as B13 and R13, we obtain the innermost, purple contours. However, the main results in this paper assume a new weak lensing-based prior on the X-ray scaling relation normalization, which changes the central value by 10% and increases the 1σ uncertainty slightly from 9% to 11%. The σ_8-Ω_m constraints using this prior and the current cluster data are shown by the light-blue contours.

with redshift. This is further discussed in the context of dark energy in Section 6.5.

In addition to their effect on the true abundance of clusters as a function of mass and redshift, cosmological parameters also affect the cluster observables through their influence on the SZ and X-ray scaling relations. Specifically, while the mass estimate inferred from the ζ–M relation depends weakly on redshift, the mass estimate inferred from the Y_X–M scaling relation depends strongly on the angular diameter distance to the cluster.

6.2. ΛCDM

In this section, we present constraints on the parameters of the ΛCDM model. Because not all parameters of this model are well constrained by cluster counts alone, we adopt priors on some of the six cosmological parameters ($\Omega_b h^2$, $\Omega_c h^2$, θ_s, n_s, A_s, and τ, defined in Section 5.1), in addition to the priors on the scaling relation parameters (A_{SZ}, B_{SZ}, C_{SZ}, and $\sigma_{\ln\zeta}$, described in Section 2.1.1, as well as A_X, B_X, C_X, $\sigma_{\ln Y_X}$, and ρ_{ζ,Y_X}, described in Section 4.1). The cluster likelihood is insensitive to the optical depth to reionization τ as well as to the primordial scalar spectrum power-law index n_s, once an appropriate pivot point is chosen. Therefore, when discussing cluster constraints without the inclusion of CMB temperature power spectrum data, we fix these parameters to the best-fit values from Planck Collaboration et al. (2014a).

These two prior constraints, in addition to the H_0 and BBN priors discussed in 5.3, leave us two remaining degrees of freedom in the ΛCDM model, which we choose to express as Ω_m and σ_8 (though in exploring the likelihood surface we actually vary the base parameters $\Omega_b h^2$, $\Omega_c h^2$, $\ln 10^{10} A_s$ and H_0). We fix the species-summed neutrino mass Σm_ν to 0.06 eV, the minimum allowed value from terrestrial measurements of squared neutrino mass differences (see e.g., Gonzalez-Garcia et al. 2012 for a review). Figure 2 shows the constraints on σ_8 and Ω_m from B13, R13, and this work. The large increase in the number of clusters primarily reduces the uncertainty on Ω_m by constraining the shape of the halo mass function. The uncertainty on the parameter combination $\sigma_8 (\Omega_m/0.27)^{0.3}$ is set by the knowledge of the overall mass scale, rather than the number of clusters, since Poisson errors on this number are subdominant. The improvement in the $\sigma_8 (\Omega_m/0.27)^{0.3}$ constraint results from the increase in the number of clusters with *Chandra* follow-up data. These two effects result in tighter joint constraints on the two parameters than we obtained in previous cluster analyses, if we use the same prior on the observable-mass relations. This can be seen in Figure 2: the innermost, purple contours use the current cluster sample and the same observable-mass priors as B13 and R13. However, in contrast to B13 and R13 we choose to use a WL-based prior on the overall mass scale for our baseline results, as discussed in 4.2. This results in slightly degraded constraints, in particular on σ_8, as can be seen from the light-blue contours in Figure 2. With the current cluster sample, the stated priors on cosmological parameters, and the updated priors on the observable-mass relations, we obtain

$$\sigma_8 = 0.784 \pm 0.039, \tag{16}$$

$$\Omega_m = 0.289 \pm 0.042, \tag{17}$$

and

$$\sigma_8 (\Omega_m/0.27)^{0.3} = 0.797 \pm 0.031. \tag{18}$$

The ΛCDM parameter constraints, including scaling relation parameters, are shown in Table 3.

In the left- and right-hand panels of Figure 3 we show the cluster abundance as a function of redshift and detection significance, respectively. Both show one-dimensional representations of the observable-space mass function. The data points, with approximate ($\sqrt{N}$) error bars shown, are independent of cosmological and scaling relation parameters. The points are independent between bins for $dN/d\xi$, and nearly independent for dN/dz, where clusters without spectroscopic redshift information can contribute to multiple bins.

Shifts in the parameters σ_8 and A_{SZ} result in roughly global shifts in the amplitude of both curves, simultaneously. The scaling relation parameter B_{SZ} induces a roughly power-law tilt in $dN/d\xi$, and parameters such as C_{SZ} and Ω_m induce tilts in dN/dz. This visualization shows two important ways in which the model, marginalized over a large number of scaling relation and cosmological parameters, is tested for agreement with the data.

Figure 4 shows the cluster constraints on the ΛCDM model in the σ_8-Ω_m plane, when combined with either the H_0+BBN prior or the BAO+θ_s+BBN prior. We also show the constraints from CMB power spectrum measurements from *Planck*+WP and *WMAP*9+S13 data. The 68% confidence regions from the cluster constraints and the CMB power spectrum constraints overlap. We proceed to adopt the *Planck*+WP data set as the baseline CMB data set for the remainder of this work. We also combine the SPT$_{CL}$+*Planck*+WP+BAO data sets to obtain joint ΛCDM parameter constraints. Finally, we note that the σ_8 constraint obtained using the SPT$_{CL}$ data in Table 3 is within 1σ of the value recently reported by the Planck collaboration for the full-mission data (their 2015 TT+lowP+lensing data set) of $\sigma_8 = 0.815 \pm 0.009$.

Table 3
Constraints on Cosmological and Scaling Relation Parameters Assuming a ΛCDM Cosmology

Parameter	Prior	$SPT_{CL}+H_0+BBN$	$SPT_{CL}+BAO+BBN$	$SPT_{CL}+Planck+WP+BAO$
A_{SZ}	5.38 ± 1.61	4.842 ± 0.913	4.936 ± 0.955	3.531 ± 0.273
B_{SZ}	1.340 ± 0.268	1.668 ± 0.083	1.660 ± 0.064	1.661 ± 0.060
C_{SZ}	0.49 ± 0.49	0.550 ± 0.315	0.864 ± 0.159	0.733 ± 0.123
$\sigma_{\ln\zeta}$	0.13 ± 0.13	0.199 ± 0.069	0.201 ± 0.070	0.203 ± 0.066
A_X	6.38 ± 0.61	6.235 ± 0.514	6.316 ± 0.505	7.030 ± 0.341
B_X	0.57 ± 0.03	0.491 ± 0.023	0.493 ± 0.023	0.498 ± 0.021
C_X	-0.40 ± 0.20	-0.251 ± 0.127	-0.280 ± 0.122	-0.174 ± 0.102
$\sigma_{\ln Yx}$	0.12 ± 0.08	0.162 ± 0.070	0.160 ± 0.069	0.154 ± 0.064
$\rho_{\zeta,Yx}$	$[-0.98, 0.98]$	-0.147 ± 0.458	-0.136 ± 0.465	-0.204 ± 0.443
Ω_m	⋯	0.289 ± 0.042	0.306 ± 0.010	0.304 ± 0.007
σ_8	⋯	0.784 ± 0.039	0.768 ± 0.030	0.820 ± 0.009
$\sigma_8 (\Omega_m/0.27)^{0.3}$	⋯	0.797 ± 0.031	0.797 ± 0.030	0.850 ± 0.013

6.2.1. Constraints on Scaling Relation Parameters

While the main focus of this work is on the cosmological constraints, the nuisance parameters are of interest themselves, both in terms of the cluster scaling relation parameter constraints and their degeneracy with the cosmological parameters. In Figure 5, we show the marginalized posterior in the multi-dimensional parameter space.

The dominant systematic uncertainty limiting the cosmological constraints from the SPT-SZ cluster sample is the uncertainty of the overall cluster mass scale. This can be seen as a strong degeneracy between A_X and $\sigma_8 (\Omega_m/0.27)^{0.3}$, which are 85% correlated given the $SPT_{CL}+H_0+BBN$ data set. The second most important source of systematic uncertainty in the cosmological constraints is from the parameter characterizing the redshift evolution of the scaling relation, C_{SZ}. In a ΛCDM cosmology, it is highly degenerate with Ω_m, correlated at 87% when considering the $SPT_{CL}+H_0+BBN$ data set.

The parameters that shift most significantly away from their priors are the B_{SZ} and B_X parameters which encode the power-law slopes of the scaling relations. We find that the preference for high B_{SZ} persists when the X-ray data are not used. In addition, this preference is not localized to any particular region of the data; when considering half the cluster sample at a time, either by redshift, ξ, or γ_{field}, the high B_{SZ} persists, albeit at a lower significance.

This high B_{SZ} implies that the measured observable-space mass function, $dN/d\xi$, is shallower than expected given the scaling relation found from the simulations described in Section 2.2. We can approximately quantify this by assuming $dN/d\xi$ follows a power law. The data prefer a power-law index of ∼4.0, compared to the simulation prediction of ∼5.0, which is disfavored by the measured $dN/d\xi$ at $\sim 4.5\sigma$.

The preference for a higher B_{SZ}, i.e., a steeper ζ–M relation, is statistically weak, approximately 1σ, due to the relatively weak 20% width assumed on the B_{SZ} prior. By contrast, the assumed width of the prior on the X-ray scaling relation slope B_X is 5%, leading to a tension between the likelihood and the prior of approximately 4σ. There is some evidence for a similarly steep Y_X–M scaling relation from the comparison of the V09 and H15 WL mass estimates in Figure 1, which prefers $B_X \sim 0.42$. Such a slope would be in $\sim 4\sigma$ tension with the expected self-similar cluster slope of $B_X = 0.6$.

In this work, we will assume that our observational priors on the Y_X–M slope and theoretical priors on the mass function slope are well motivated, but note that the shape of the observable-space mass function will need to be studied in more detail for future work.

6.3. ΛCDM + Σm_ν

We now consider a cosmological model in which the species-summed neutrino mass Σm_ν is a free parameter. Constraints on this model from the CMB power spectrum show a strong degeneracy between σ_8 and Σm_ν (e.g., Komatsu et al. 2009; Planck Collaboration et al. 2014a; Abazajian et al. 2015). This allows even modest measurements of σ_8 to improve on neutrino mass constraints from the CMB power spectrum data alone. Figure 6 shows the improvement in constraints when adding cluster abundance information to CMB power spectrum data alone (*Planck*+WP), and also when including BAO data. In both cases, the addition of cluster information tightens the constraint and causes the posterior to peak at positive values of Σm_ν, though the 95% upper limit on Σm_ν remains largely unchanged. Allowing the Σm_ν to vary in the range of 0–2 eV, and using the combination of the $SPT_{CL}+Planck+WP+BAO$ data sets, we find

$$\Sigma m_\nu = 0.14 \pm 0.08 \text{eV}. \quad (19)$$

We note that the preference for positive Σm_ν, when we combine our cluster abundance measurements with *Planck* data, is driven by the small residual tension between the preferred values of σ_8 in the two data sets. Such a preference has been pointed out by several authors (e.g., Battye & Moss 2014; Planck Collaboration et al. 2014b; Wyman et al. 2014), but is in contrast to the preference for positive Σm_ν shown, for example, by the combination of *WMAP*+SPT CMB power spectrum data and SPT cluster data in Hou et al. (2014), in which the evidence for positive Σm_ν is not driven by the cluster data. In this work, we find relatively good agreement between the preferred σ_8 using the CMB and SPT_{CL} data sets, so the preference for positive Σm_ν is weak and consistent at 1σ with the minimum expected value of ∼0.06 eV from neutrino oscillation experiments (Lesgourgues & Pastor 2006). Relative to the previous cluster-based constraints cited above, the updated WL-based calibration described in Section 4.2, has shifted the normalization and increased the uncertainty of the observable-mass relation in a way that relieves tension with the *Planck* CMB data (see Figure 2). We also note that our constraint on Σm_ν is largely independent of the change in the optical depth to reionization, τ, between the *Planck* 2013 and 2015 data release; the SPT_{CL} constraints are independent of τ,

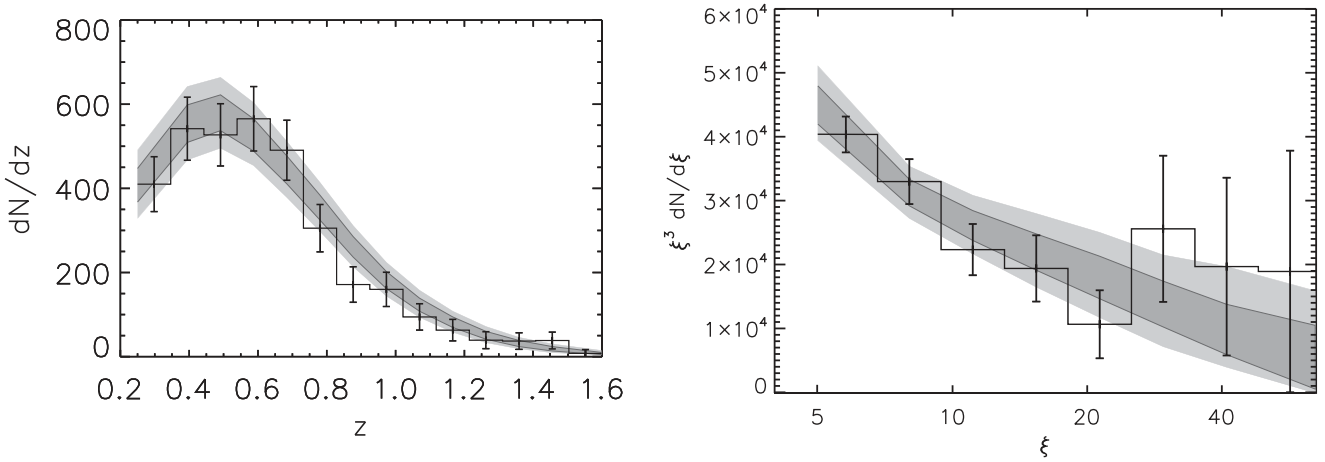

Figure 3. Number density of clusters as a function of redshift (left panel) and of the SPT-SZ mass proxy ξ (right panel). The data points show the measured abundance with $\sqrt{N}$ error bars. The grey bands show the 68% and 95% allowed model ranges after marginalizing over all cosmological and scaling relation parameters in the ΛCDM model with the SPT$_{\rm CL}$+H_0+BBN data set. In the right-hand panel, the ξ axis is shown on a logarithmic scale and the abundance axis has been multiplied by three powers of ξ in order to visualize the abundance over a range of ξ values despite the extreme steepness of the measured mass function.

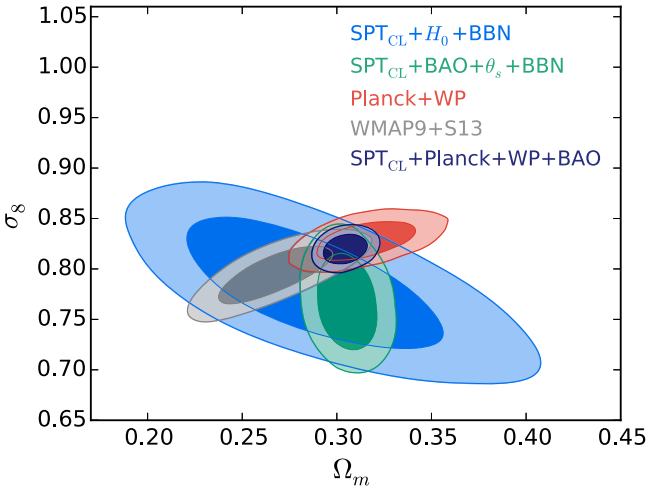

Figure 4. Comparison of cluster constraints on σ_8 and Ω_m to constraints from primary CMB anisotropies, assuming a ΛCDM cosmology. The cluster constraints, when combined with either the H_0 or BAO+θ_s prior, are in agreement with the CMB data sets.

and the *Planck* CMB constraints on σ_8 and Ω_m negligibly changed between the two data releases.

6.4. ΛCDM + Σm_ν + $N_{\rm eff}$

The effective number of relativistic species, $N_{\rm eff}$, affects the CMB power spectrum by altering the time of matter–radiation equality, changing the apparent sound horizon at recombination (e.g., Hou et al. 2013). This mechanism results in strong degeneracies between $N_{\rm eff}$ and other cosmological parameters, notably H_0 and σ_8, when considering CMB data alone (e.g., Bashinsky & Seljak 2004). Thus, the addition of constraints on σ_8—such as from the cluster data in this work—and H_0 can improve upon CMB-only constraints on $N_{\rm eff}$.

Here, we consider simultaneously varying the species-summed neutrino mass and the effective number of relativistic species. In this cosmological model, the *Planck*+WP data alone constrain the σ_8-Ω_m-H_0 parameter volume relatively poorly. Adding the cluster information improves on all three of those parameters by roughly a factor of two. Through parameter degeneracies, this improves the simultaneous constraints on $N_{\rm eff}$ and Σm_ν as shown in Figure 7. The simultaneous constraints are

$$N_{\rm eff} = 3.25 \pm 0.23 \quad (20)$$

and

$$\Sigma m_\nu = 0.39 \pm 0.20\ {\rm eV}, \quad (21)$$

which represent factors of 1.3 and 1.6 respective improvement over the *Planck*+WP data alone.

Adding BAO data reduces the remaining allowed parameter space significantly to $N_{\rm eff} = 3.28 \pm 0.20$ and $\Sigma m_\nu = 0.18 \pm 0.09$, and results in a degeneracy between $N_{\rm eff}$ and Σm_ν, allowing for larger values of $N_{\rm eff}$ for increasing Σm_ν. These constraints can be further tightened with the addition of local H_0 measurements, with the caveat that the best-fit value of H_0 from the SPT$_{\rm CL}$+*Planck*+WP+BAO data set, $H_0 = 68.6 \pm 1.2\ {\rm km\ s^{-1}\ Mpc^{-1}}$, is in mild tension with direct local measurements from Riess et al. (2011). Proceeding to add those local measurements, so that we consider a SPT$_{\rm CL}$+*Planck*+WP+H_0+BAO data set, we find a preference for larger $N_{\rm eff}$, resulting in the marginalized constraints of

$$N_{\rm eff} = 3.43 \pm 0.16 \quad (22)$$

and

$$\Sigma m_\nu = 0.16 \pm 0.08\ {\rm eV}. \quad (23)$$

The combined data set has a 2.3σ preference for $N_{\rm eff} > 3.046$, the standard model prediction. This is partially driven by the weak tension between local H_0 measurements and the *Planck* +BAO data set, as has been noted by other authors (e.g., Battye & Moss 2014; Hou et al. 2014; Wyman et al. 2014). However, the sensitivity to the H_0 prior is relatively weak. The preference for $N_{\rm eff}$ exceeding the standard model prediction would still be 2.0σ if the central value of the H_0 prior was reduced by one standard deviation.

This mild preference for massive neutrinos and extra $N_{\rm eff}$ has also been noted by other authors. For example, by combining CMB power spectrum data, BAO, SZ cluster counts, cosmic shear data, redshift space distortions from BOSS, and CMB lensing from *Planck*, Battye et al. (2015) found an even

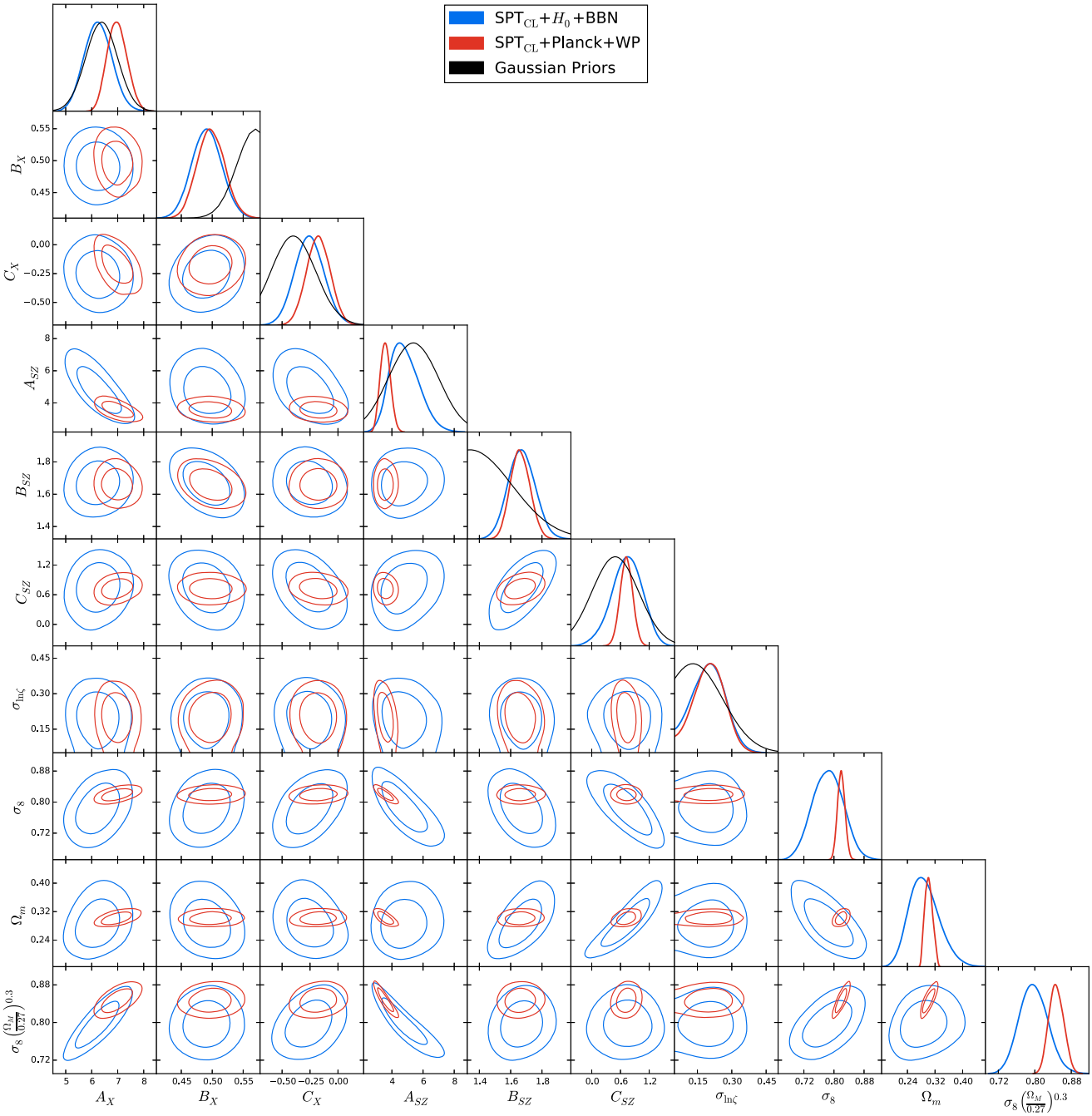

Figure 5. Contour triangle plot showing the degeneracies between scaling relation parameters and cosmological parameters. Parameters $\Omega_b h^2$, H_0, n_s, $\sigma_{\ln Y_X}$, and ρ_{ζ,Y_X} are marginalized over and not shown since they are primarily constrained by priors, or by the *Planck* data. The cluster likelihood is nearly flat over the explored range of these parameters.

stronger preference for $N_{\rm eff}$ being larger than the ΛCDM model value. In MacCrann et al. (2015), the tension between CFHTLenS cosmic shear data and *Planck*+WP in the $\Omega_m - \sigma_8$ plane is shown, and the effective number of extra neutrino species ($\Delta N_{\rm eff}$) is favored to be non-zero in the joint fit, alleviating such tension to some extent. More concretely, Ruiz & Huterer (2015) found redshift-space distortion data in $\sim 3\sigma$ tension with ΛCDM but that this tension was alleviated when the species-summed neutrino mass was made a free parameter. Another similar study has been done by Bernal et al. (2016) where adding neutrino mass reduces the tension on dark energy parameters inferred from the combination of geometry and the growth of the large-scale structure.

6.5. *wCDM*

With the increased number of clusters in this work we are able to place constraints not only on the local cluster abundance but also on the evolution of cluster abundance with redshift. In particular, we examine the constraints on the *w*CDM cosmology, where the equation of state of dark energy w is a free parameter. We assume that w is a constant (i.e., its value does not evolve with redshift). This additional parameter affects the cluster abundance and observables through its

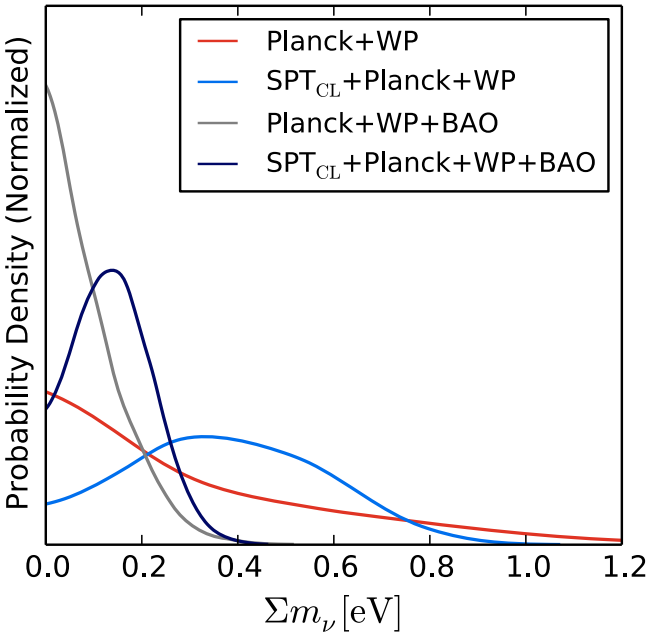

Figure 6. Constraints on the species-summed neutrino mass. The addition of cluster constraints to either the *Planck*+WP or *Planck*+WP+BAO data sets has a similar effect: the posterior peaks at positive values, but remains consistent with zero.

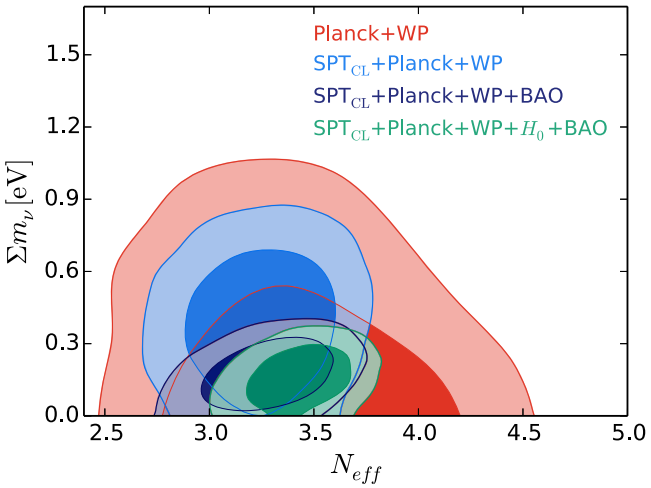

Figure 7. Simultaneous constraints on the effective number of relativistic species and the species-summed neutrino mass. The addition of the SPT cluster data reduces the allowed parameter space.

influence on the geometry of the universe and, more importantly, the growth of structure. The geometrical effects include the change in the survey volume element and the angular diameter distance that modifies the implied X-ray mass information. However, in contrast to other probes of dark energy, the cluster abundance measurement is very sensitive to the effect of w on the growth of structure, primarily $\sigma_8(z)$ (e.g., Wang & Steinhardt 1998; Haiman et al. 2001).

In Figure 8, we show constraints on the dark energy equation of state parameter w and the energy density of dark energy today $\Omega_{\rm DE}$ for different cosmological probes. With the SPT$_{\rm CL}$+H_0+BBN data set, we obtain

$$w = -1.28 \pm 0.31 \quad (24)$$

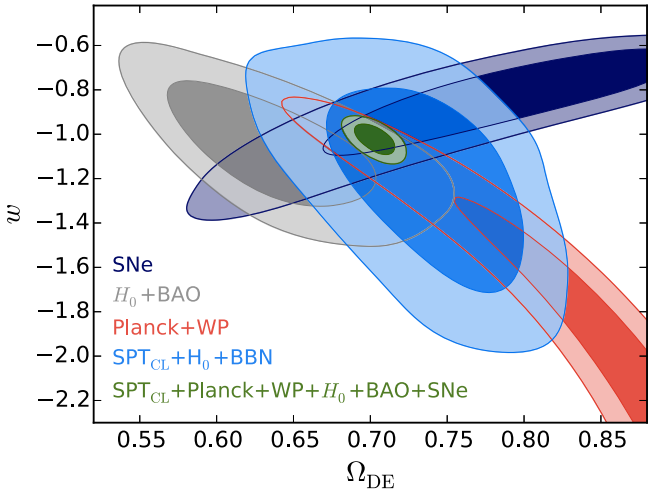

Figure 8. Comparison of different cosmological probes of dark energy. The countours show the simultaneous constraints on the present-day density of dark energy $\Omega_{\rm DE} = 1 - \Omega_m$ and the dark energy equation of state parameter w. Using priors on H_0 and $\Omega_b h^2$, the SPT cluster data are able to simultaneously constrain the two parameters, and are in good agreement with the other probes. The other probes are sensitive to dark energy primarily through its effect on the geometry of the universe.

and

$$\Omega_{\rm DE} = 0.738 \pm 0.046. \quad (25)$$

This is in good agreement, and of comparable precision, with the constraints when considering other cosmological probes, including *Planck*+WP, BAO, and SNe, as can be seen in Figure 8. Since all these probes except the cluster abundance measurement are primarily geometrical tests in this plane, the consistency between the cluster-implied parameter constraints, and those from other data sets, offers an important systematic test of dark energy. This measurement is limited primarily by our knowledge of the redshift evolution of the ζ–M scaling relation, $C_{\rm SZ}$. Specifically, both Ω_m and w are correlated with $C_{\rm SZ}$ at the $\sim$60% level, whereas the correlation with $A_{\rm X}$ is only $\sim$30%.

As shown in Figure 9, the *Planck*+WP measurements of the primary CMB show a strong degeneracy between w and σ_8. The addition of cluster data breaks the degeneracy and results in the marginalized constraints

$$w = -1.04 \pm 0.17 \quad (26)$$

and

$$\sigma_8 = 0.803 \pm 0.045. \quad (27)$$

This level of w-uncertainty is $\sim$2.5 times larger compared to the constraints when adding either of the BAO or SNe data sets to the *Planck*+WP measurements (Aubourg et al. 2015; Betoule et al. 2014).

For the data set combination H_0+BAO+SNe, which does not include primary CMB data, σ_8 is not determined. Adding the cluster data improves the w constraint by 37% through a direct measurement of the dark energy parameters w and $\Omega_{\rm DE}$, rather than by breaking the w-σ_8 degeneracy. For this combination, we find

$$w = -1.08 \pm 0.07. \quad (28)$$

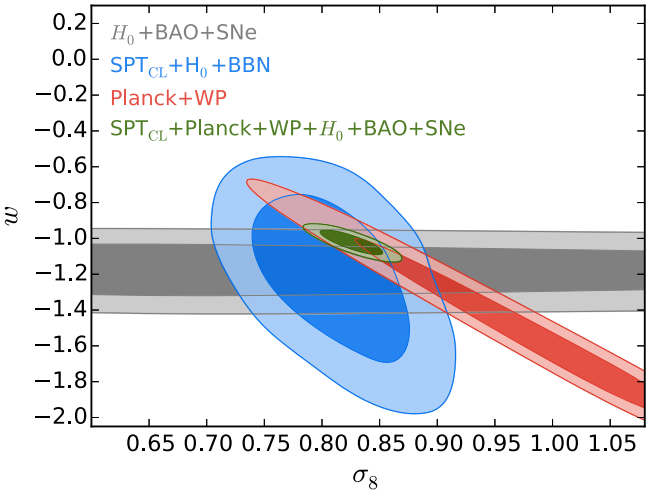

Figure 9. Combined constraints on w and σ_8. The CMB power spectrum data from *Planck*+WP shows a strong degeneracy, while the purely geometric constraints from H_0+BAO+SNe do not constrain σ_8. The cluster data simultaneously constrains the two parameters, improving the joint CMB+-H_0+BAO+SNe constraints both through breaking the w-σ_8 degeneracy present in the CMB constraints, and the direct measurement of w.

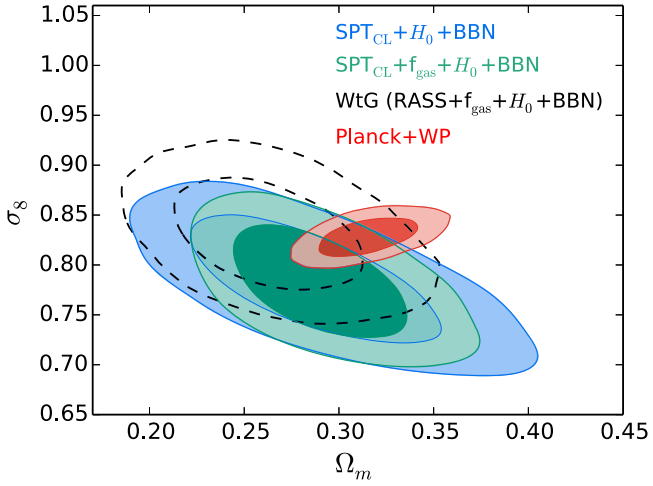

Figure 10. Comparison of the constraints on σ_8 and Ω_m from this work, Weighing the Giants (WtG), and *Planck*+WP CMB measurements. We also show the results from this work after adding the approximate parameter constraints from the f_{gas} analysis of Mantz et al. (2014) for a more direct comparison to the WtG cluster constraints.

Finally, when considering the *Planck*+WP+H_0+BAO+SNe data sets, w is constrained to -1.062 ± 0.048. The allowed parameter space shows a significant w-σ_8 degeneracy, which allows the addition of the cluster data to improve this constraint by 14%, to

$$w = -1.023 \pm 0.042, \quad (29)$$

consistent with ΛCDM where $w = -1$.

7. COMPARISON TO OTHER CLUSTER SURVEYS

In this section, we compare the SPT$_{CL}$ cosmological constraints to results using other cluster surveys. We focus on the ΛCDM constraints from Section 6.2, which employed a SPT$_{CL}$+H_0+BBN data set, and where we constrained $\sigma_8 (\Omega_m/0.27)^{0.3} = 0.797 \pm 0.031$ and $\sigma_8 = 0.784 \pm 0.039$. When comparing to other results, we will discuss differences where appropriate.

Other SZ cluster-based constraints include results from the Atacama Cosmology Telescope (ACT, Hasselfield et al. 2013) and *Planck* (Planck Collaboration et al. 2014b, 2015) cluster surveys. However, comparisons to both are complicated by differences in the assumed mass calibration. In Hasselfield et al. (2013), the ACT collaboration reported cosmological constraints using 15 SZ-selected clusters between $0.2 < z < 1.4$. Several sets of constraints were presented, which assumed different priors on the SZ-scaling parameters and also included a calibration based on the dynamical mass measurements from Sifón et al. (2013). The latter relied on a scaling relation between velocity dispersion and cluster mass, which was later found to be biased high by ∼20% when using more recent simulations (Kirk et al. 2015). Using a fixed SZ-scaling relation based on the simulations from Battaglia et al. (2012) i.e., without including any uncertainty in the cluster mass calibration, the ACT$_{CL}$+H_0+BBN data set was used to constrain $\sigma_8 (\Omega_m/0.27)^{0.3} = 0.848 \pm 0.032$ and $\sigma_8 = 0.872 \pm 0.065$, consistent with the constraints presented in this work.

The *Planck* collaboration has produced two cluster-based cosmological analyses (Planck Collaboration et al. 2014b, 2015). Planck Collaboration et al. (2014b) used a sample of 189 SZ-selected clusters between $0.0 < z < 0.55$ with a median redshift of 0.15, which is lower than the SPT cluster sample due to the *Planck* selection function. Assuming an identical H_0+BBN data set to our work and assuming a fixed scaling relation except for an overall mass-bias factor b with a uniform prior between 0.7 and 1.0, they constrained $\sigma_8 (\Omega_m/0.27)^{0.3} = 0.774 \pm 0.024$ and $\sigma_8 = 0.77 \pm 0.03$, consistent with our results. In Planck Collaboration et al. (2015), the previous scaling relation calibration was compared to more recent WL measurements (H15, WtG), which are also used in this work. For example, H15 found a mass-bias factor of 0.76 ± 0.08 for the *Planck* clusters in their lensing sample. While no numerical constraints were given, the newer *Planck* constraints were found to be consistent with the previous *Planck* results, and are also visually in good agreement with our results using this mass-bias factor.

In addition, our cosmological constraints are consistent with other previous cluster surveys, including constraints from the X-ray selected sample from Vikhlinin et al. (2009b) and the optically selected sample from Rozo et al. (2010).

Finally, we compare to more recent cosmological constraints from WtG (Mantz et al. 2015). Their baseline constraints incorporate a cluster sample selected from the *ROSAT* All-Sky Survey (RASS), follow-up X-ray observations from *Chandra*, including cosmological constraints from cluster gas-fraction (f_{gas}, see Mantz et al. 2014) measurements, and WL data from WtG, a sub-set of which we used to estimate our cluster mass calibration in Section 4.2. In Figure 10, we compare directly to the WtG constraints in the σ_8–Ω_m plane (WtG find marginalized constraints of $\sigma_8 = 0.830 \pm 0.035$ and $\Omega_m = 0.259 \pm 0.030$). We also plot the SPT$_{CL}$ constraints with an additional prior of $\Omega_b/\Omega_m h^{1.5} = 0.089 \pm 0.012$, to mimic the f_{gas} constraints.

Overall, we find good agreement between our SPT$_{CL}$ data set and both the *Planck*-CMB and WtG data. The agreement between the WtG and SPT$_{CL}$ constraints is impressive considering the different selection methods (SZ versus X-ray), the different X-ray observable (Y_X versus gas mass)

and corresponding observable-mass scaling relation, as well as the independent X-ray analysis pipelines. This agreement extends to the wCDM cosmological model. For example, using the WtG cluster data (including $f_{\rm gas}$ measurements), Mantz et al. (2015) constrain $w = -0.98 \pm 0.15$, consistent with the results in Section 6.5. The combination of the two cluster data sets is potentially very powerful for improving cluster-based constraints due to the different redshift ranges of each sample; the majority of the WtG sample is at $z < 0.25$, below the lower redshift cut of the $\rm SPT_{CL}$ sample used in this work. This is particularly important for cluster-based constraints on dark energy because the combined data sets would provide improved constraints on the evolution of the cluster mass function. This complementarity was also noted in Mantz et al. (2015), who estimated that the combined data sets could improve the WtG cluster-based constraints on dark energy and modified gravity by a factor of >2.

8. CONCLUSION

In this work, we have taken a well-defined subsample of the SPT cluster catalog from Bleem et al. (2015), selecting only for redshift $z > 0.25$ and SPT-SZ detection significance $\xi > 5$. In order to obtain cosmological constraints, we combine this cluster catalog with *Chandra* X-ray observations for 82 clusters. In addition, we adopt a purely WL-based prior on the overall mass scale of the sample from a reanalysis of Vikhlinin et al. (2009b) using the more recent WL mass estimates from Hoekstra et al. (2015) and the Weighing the Giants (WtG) project (Applegate et al. 2014; Kelly et al. 2014; von der Linden et al. 2014a; Mantz et al. 2015). The 1σ width of this prior is 10%, which is limited by the small number of clusters in the reanalysis.

The computation of the cluster likelihood uses a new algorithm that scales linearly with the number of mass proxies, where previous algorithms scaled exponentially, which makes incorporating more mass proxies such as WL shear, velocity dispersions, and/or multiple X-ray mass proxies computationally tractable. Our algorithm includes the option to marginalize over all possible correlations between the observables.

Assuming a ΛCDM cosmology and combining with H_0+BBN, we find the marginalized constraints $\sigma_8 = 0.784 \pm 0.039$ and $\Omega_m = 0.289 \pm 0.042$. The combined parameter combination $\sigma_8 (\Omega_m/0.27)^{0.3}$ is constrained to 0.797 ± 0.031. We find good agreement with the parameter constraints obtained from the WtG project, as well as CMB constraints from either *WMAP*9+S13 (Hinshaw et al. 2013; Story et al. 2013) or *Planck*+WP (Planck Collaboration et al. 2014a). We proceed to adopt *Planck*+WP as our baseline CMB data set.

We consider several extensions to the ΛCDM model. When we allow the species-summed neutrino mass to be a free parameter, the addition of cluster information to CMB information causes the posterior to peak at positive values of neutrino mass (though it is consistent with zero). The same behavior is seen when combining with CMB+BAO, yielding $\Sigma m_\nu = 0.14 \pm 0.08$ eV. When further allowing the effective number of relativistic species $N_{\rm eff}$ to be a free parameter, and combining with CMB+H_0+BAO, we find $N_{\rm eff} = 3.43 \pm 0.16$ and $\Sigma m_\nu = 0.16 \pm 0.08$ eV.

Finally, when the dark energy equation of state parameter w is allowed to be free, this cluster catalog can be combined only with priors on H_0 and $\Omega_b h^2$ to measure $w = -1.28 \pm 0.31$, showing good consistency with the ΛCDM cosmological model. Adding the cluster data to CMB+H_0+BAO+SNe improves the w constraint to $w = -1.023 \pm 0.042$.

The full cosmological power of the 2500 square-degree SPT-SZ cluster survey has not yet been realized. A joint analysis of the WtG and SPT-SZ cluster samples is currently being performed. In addition, weak-lensing observations of SPT-SZ discovered clusters themselves are currently being analyzed and are expected to improve on the 10% mass normalization uncertainty in this paper, in turn sharpening the cosmological constraints. Especially important is accurate knowledge of the mass scale over a range of redshifts, which would specifically improve constraints on models of dark energy or modified gravity.

The SPT is presently reobserving a 500 square-degree patch of the SPT-SZ survey area with the polarization-sensitive receiver SPTpol (Austermann et al. 2012). While the primary science goals are related to polarization, the greater map depth allows for a lower cluster mass threshold, therefore extending the survey out to higher redshift. The next receiver, SPT-3G (Benson et al. 2014), is currently being built and will allow for significant progress in the SPT cluster program. The SPT-3G receiver will have a mapping speed ∼20 times higher than SPTpol, which should yield ∼5000 cluster detections and, importantly, allow cluster mass calibration through CMB-cluster lensing (e.g., Baxter et al. 2015; Melin & Bartlett 2015; Seljak & Zaldarriaga 2000).

The South Pole Telescope is supported by the National Science Foundation through grant PLR-1248097. Partial support is also provided by the NSF Physics Frontier Center grant PHY-1125897 to the Kavli Institute of Cosmological Physics at the University of Chicago, the Kavli Foundation and the Gordon and Betty Moore Foundation grant GBMF 947. This work used resources of McGill University's High Performance Computing centre, a part of Compute Canada. This work was supported in part by the Kavli Institute for Cosmological Physics at the University of Chicago through grant NSF PHY-1125897 and an endowment from the Kavli Foundation and its founder Fred Kavli. This work was supported in part by the US Department of Energy under contract number DE-AC02-76SF00515. The McGill group acknowledges funding from the National Sciences and Engineering Research Council of Canada, Canada Research Chairs program, and the Canadian Institute for Advanced Research. TdH is supported by a Miller Research Fellowship, as well as receiving support from a Natural Science and Engineering Research Council of Canada Postgraduate Scholarship-Doctoral award. BB is supported by the Fermi Research Alliance, LLC under Contract No. De-AC02-07CH11359 with the United States Department of Energy. Argonne National Laboratorys work was supported under U.S. Department of Energy contract DE-AC02-06CH11357. DA and TS acknowledge support from the German Federal Ministry of Economics and Technology (BMWi) provided through DLR under projects 50 OR 1210 and 50 OR 1407. RJF gratefully acknowledges support from the Alfred P. Sloan Foundation. CR acknowledges support from the University of Melbourne and from the Australian Research Council's Discovery Projects scheme (DP150103208). JHL is supported by NSERC through the discovery grant and Canada Research Chair programs, as well as FRQNT. The Munich group acknowledges the support

of the DFG Cluster of Excellence "Origin and Structure of the universe" and the Transregio program TR33 "The Dark universe." The Dark Cosmology Centre is funded by the Danish National Research Foundation. Optical and infrared followup of SPT Clusters at the Harvard-Smithsonian Center for Astrophysics was supported by NSF grant ANT-1009649.

REFERENCES

Abazajian, K. N., Arnold, K., Austermann, J., et al. 2015, APh, 63, 66
Acquaviva, V., & Gawiser, E. 2010, PhRvD, 82, 082001
Allen, S. W., Evrard, A. E., & Mantz, A. B. 2011, ARA&A, 49, 409
Anderson, L., Aubourg, É., Bailey, S., et al. 2014, MNRAS, 441, 24
Andersson, K., Benson, B. A., Ade, P. A. R., et al. 2011, ApJ, 738, 48
Applegate, D. E., von der Linden, A., Kelly, P. L., et al. 2014, MNRAS, 439, 48
Aubourg, E., Bailey, S., Bautista, J. E., et al. 2015, PhRvD, 92, 123516
Austermann, J. E., Aird, K. A., Beall, J. A., et al. 2012, Proc. SPIE, 8452, 8452E
Bahcall, N. A., & Cen, R. 1992, ApJL, 398, L81
Bashinsky, S., & Seljak, U. 2004, PhRvD, 69, 083002
Battaglia, N., Bond, J. R., Pfrommer, C., & Sievers, J. L. 2012, ApJ, 758, 74
Battye, R. A., Charnock, T., & Moss, A. 2015, PhRvD, 91, 103508
Battye, R. A., & Moss, A. 2014, PhRvL, 112, 051303
Baxter, E. J., Keisler, R., Dodelson, S., et al. 2015, ApJ, 806, 247
Benson, B. A., Ade, P. A. R., Ahmed, Z., et al. 2014, Proc. SPIE, 9153, 9153A
Benson, B. A., de Haan, T., Dudley, J. P., et al. 2013, ApJ, 763, 147
Bernal, J. L., Verde, L., & Cuesta, A. J. 2016, JCAP, 2, 059
Betoule, M., Kessler, R., Guy, J., et al. 2014, A&A, 568, A22
Bhattacharya, S., Heitmann, K., White, M., et al. 2011, ApJ, 732, 122
Bleem, L. E., Stalder, B., de Haan, T., et al. 2015, ApJS, 216, 27
Bocquet, S., Saro, A., Mohr, J. J., et al. 2015, ApJ, 799, 214
Brodwin, M., Ruel, J., Ade, P. A. R., et al. 2010, ApJ, 721, 90
Carlstrom, J. E., Holder, G. P., & Reese, E. D. 2002, ARA&A, 40, 643
Carlstrom, J. E., Ade, P. A. R., Aird, K. A., et al. 2011, PASP, 123, 568
Cooke, R. J., Pettini, M., Jorgenson, R. A., Murphy, M. T., & Steidel, C. C. 2014, ApJ, 781, 31
Costanzi, M., Villaescusa-Navarro, F., Viel, M., et al. 2013, JCAP, 12, 12
Evrard, A. E., Metzler, C. A., & Navarro, J. F. 1996, ApJ, 469, 494
Evrard, A. E., Bialek, J., Busha, M., et al. 2008, ApJ, 672, 122
Fazio, G. G., Hora, J. L., Allen, L. E., et al. 2004, ApJS, 154, 10
Gonzalez-Garcia, M. C., Maltoni, M., Salvado, J., & Schwetz, T. 2012, JHEP, 12, 123
Haiman, Z., Mohr, J. J., & Holder, G. P. 2001, ApJ, 553, 545
Hasselfield, M., Hilton, M., Marriage, T. A., et al. 2013, JCAP, 7, 8
Hinshaw, G., Larson, D., Komatsu, E., et al. 2013, ApJS, 208, 19
Hoekstra, H. 2007, MNRAS, 379, 317
Hoekstra, H., Herbonnet, R., Muzzin, A., et al. 2015, MNRAS, 449, 685
Hoekstra, H., Mahdavi, A., Babul, A., & Bildfell, C. 2012, MNRAS, 427, 1298
Holder, G. 2006, arXiv:astro-ph/0602251
Holder, G. P., & Carlstrom, J. E. 2001, ApJ, 558, 515
Hou, Z., Keisler, R., Knox, L., Millea, M., & Reichardt, C. 2013, PhRvD, 87, 083008
Hou, Z., Reichardt, C. L., Story, K. T., et al. 2014, ApJ, 782, 74
Hu, W., & Kravtsov, A. V. 2003, ApJ, 584, 702
Ishak, M., Upadhye, A., & Spergel, D. N. 2006, PhRvD, 74, 043513
Keisler, R., Reichardt, C. L., Aird, K. A., et al. 2011, ApJ, 743, 28
Kelly, B. C. 2007, ApJ, 665, 1489
Kelly, P. L., von der Linden, A., Applegate, D. E., et al. 2014, MNRAS, 439, 28
Kirk, B., Hilton, M., Cress, C., et al. 2015, MNRAS, 449, 4010
Komatsu, E., Dunkley, J., Nolta, M. R., et al. 2009, ApJS, 180, 330
Kravtsov, A. V., Vikhlinin, A., & Nagai, D. 2006, ApJ, 650, 128
Le Brun, A. M. C., McCarthy, I. G., Schaye, J., & Ponman, T. J. 2014, MNRAS, 441, 1270
Lesgourgues, J., & Pastor, S. 2006, PhR, 429, 307
Lewis, A., & Bridle, S. 2002, PhRvD, 66, 103511
Lewis, A., Challinor, A., & Lasenby, A. 2000, ApJ, 538, 473
MacCrann, N., Zuntz, J., Bridle, S., Jain, B., & Becker, M. R. 2015, MNRAS, 451, 2877
Madhavacheril, M., Sehgal, N., Allison, R., et al. 2015, PhRvL, 114, 151302
Mantz, A., Allen, S. W., Ebeling, H., & Rapetti, D. 2008, MNRAS, 387, 1179
Mantz, A., Allen, S. W., Rapetti, D., & Ebeling, H. 2010, MNRAS, 406, 1759
Mantz, A. B., Allen, S. W., Morris, R. G., et al. 2014, MNRAS, 440, 2077
Mantz, A. B., von der Linden, A., Allen, S. W., et al. 2015, MNRAS, 446, 2205
McDonald, M., Benson, B., Veilleux, S., Bautz, M. W., & Reichardt, C. L. 2013a, ApJL, 765, L37
McDonald, M., Benson, B. A., Vikhlinin, A., et al. 2013b, ApJ, 774, 23
Melin, J.-B., & Bartlett, J. G. 2015, A&A, 578, A21
Mohr, J. J. 2005, ASP Conf. Ser. 339, Observing Dark Energy, ed. S. C. Wolff & T. R. Lauer (San Francisco, CA: ASP), 140
Mortonson, M. J., Hu, W., & Huterer, D. 2009, PhRvD, 79, 023004
Mortonson, M. J., Hu, W., & Huterer, D. 2010, PhRvD, 81, 063007
Motl, P. M., Hallman, E. J., Burns, J. O., & Norman, M. L. 2005, ApJL, 623, L63
Munari, E., Biviano, A., Borgani, S., Murante, G., & Fabjan, D. 2013, MNRAS, 430, 2638
Nagai, D., Kravtsov, A. V., & Vikhlinin, A. 2007, ApJ, 668, 1
Planck Collaboration, et al. 2014a, A&A, 571, A16
Planck Collaboration, et al. 2014b, A&A, 571, A20
Planck Collaboration, et al. 2015, arXiv:1502.01597
Press, W., & Schechter, P. 1974, ApJ, 187, 425
Rapetti, D., Allen, S. W., Mantz, A., & Ebeling, H. 2009, MNRAS, 400, 699
Rapetti, D., Allen, S. W., Mantz, A., & Ebeling, H. 2010, MNRAS, 406, 1796
Reichardt, C. L., Stalder, B., Bleem, L. E., et al. 2013, ApJ, 763, 127
Riess, A. G., Macri, L., Casertano, S., et al. 2011, ApJ, 730, 119
Rozo, E., Wechsler, R. H., Rykoff, E. S., et al. 2010, ApJ, 708, 645
Ruel, J., Bazin, G., Bayliss, M., et al. 2014, ApJ, 792, 45
Ruiz, E. J., & Huterer, D. 2015, PhRvD, 91, 063009
Saro, A., Mohr, J. J., Bazin, G., & Dolag, K. 2013, ApJ, 772, 47
Schaffer, K. K., Crawford, T. M., Aird, K. A., et al. 2011, ApJ, 743, 90
Schechter, P. 1976, ApJ, 203, 297
Seljak, U., & Zaldarriaga, M. 2000, ApJ, 538, 57
Shirokoff, E., Reichardt, C. L., Shaw, L., et al. 2011, ApJ, 736, 61
Sifón, C., Menanteau, F., Hasselfield, M., et al. 2013, ApJ, 772, 25
Skillman, S. W., Warren, M. S., Turk, M. J., et al. 2014, arXiv:1407.2600
Song, J., Zenteno, A., Stalder, B., et al. 2012, ApJ, 761, 22
Stanek, R., Rasia, E., Evrard, A. E., Pearce, F., & Gazzola, L. 2010, ApJ, 715, 1508
Story, K. T., Reichardt, C. L., Hou, Z., et al. 2013, ApJ, 779, 86
Sunyaev, R. A., & Zel'dovich, Y. B. 1972, CoASP, 4, 173
Tinker, J., Kravtsov, A. V., Klypin, A., et al. 2008, ApJ, 688, 709
Vanderlinde, K., Crawford, T. M., de Haan, T., et al. 2010, ApJ, 722, 1180
Vanderveld, R. A., Mortonson, M. J., Hu, W., & Eifler, T. 2012, PhRvD, 85, 103518
Vikhlinin, A., Burenin, R. A., Ebeling, H., et al. 2009a, ApJ, 692, 1033
Vikhlinin, A., Kravtsov, A., Forman, W., et al. 2006, ApJ, 640, 691
Vikhlinin, A., Kravtsov, A. V., Burenin, R. A., et al. 2009b, ApJ, 692, 1060
von der Linden, A., Allen, M. T., Applegate, D. E., et al. 2014b, MNRAS, 439, 2
von der Linden, A., Mantz, M. T., Allen, S. W., et al. 2014a, MNRAS, 443, 1973
Wang, L., & Steinhardt, P. J. 1998, ApJ, 508, 483
White, S. D. M., Efstathiou, G., & Frenk, C. S. 1993, MNRAS, 262, 1023
Wyman, M., Rudd, D. H., Vanderveld, R. A., & Hu, W. 2014, PhRvL, 112, 051302
Yu, L., Nelson, K., & Nagai, D. 2015, ApJ, 807, 12
Zhan, H., Knox, L., & Tyson, J. A. 2009, ApJ, 690, 923